https://doi.org/10.5194/egusphere-2026-913
Preprint. Discussion started: 16 March 2026

Modulation of glacier surge cycles on decadal to centennial timescales by intrinsic thermal-structure variability

Andrew Nolan[1], Gwenn E. Flowers[1], Andy Aschwanden[2], and Adrien Gilbert[3]

[1]Department of Earth Sciences, Simon Fraser University, Burnaby, British Columbia, Canada
[2]Geophysical Institute, University of Alaska Fairbanks, Fairbanks, Alaska, USA
[3]IGE, Univ. Grenoble Alpes, CNRS, INRAE, IRD, Grenoble INP, 38000 Grenoble, France

Correspondence: Gwenn E. Flowers (gflowers@sfu.ca)

Abstract. Glacier surges occur across a range of geographical and environmental settings, but are favored by a climate envelope in which polythermal glaciers are common. Thermal structure is known to play a regulatory role in surge propagation, but whether surging has a long-term influence on thermal structure has been comparatively under-investigated. In this study, we analyze the intrinsic variability of glacier thermal structure associated with the surge cycle, and its potential impact on surging behavior itself, in the presence of a stationary climate. We apply a thermo-mechanically coupled Stokes ice-flow model to an idealized two-dimensional flowband glacier geometry intended to represent a class of small polythermal glaciers in Yukon, Canada, where changes in surge character have been observed and changes in thermal structure projected. The idealized glacier is largely temperate in the accumulation area and cold in the ablation area. Surge-like events are induced in the model by prescribing abrupt reductions in basal friction at 15–60-year recurrence intervals. Surging is found to produce glaciers that are, on average, both smaller and colder than their non-surge-type counterparts. When surge events are sufficiently vigorous, a secondary, thermally-driven, internal oscillation emerges that dramatically alters the magnitude and spatial extent of surge events. This oscillation reflects variations in the length of the temperate (thawed) portion of the glacier bed, induced by imbalances between horizontal advection of temperate ice and vertical conductive cooling. Its amplitude and period are a function of surge vigor, with periods ranging from ∼150–450 years. While the existence, let alone detectability, of such a secondary oscillation in a non-stationary climate may be questioned, this result motivates a more thorough attribution study of the evolution of surge character in polythermal glaciers.

1 Introduction

Glacier surges are quasi-periodic fast-flow events that have long fascinated glaciologists (e.g., Meier and Post, 1969, 1987; Truffer et al., 2021) and are recognized as part of a spectrum of ice-flow instabilities (Clarke, 1987; Lovell et al., 2026). Within glacierized regions where surging occurs, surges are associated with natural hazards (e.g., Björnsson, 2010; Bazai et al., 2021; Lovell et al., 2026), impact water resources (e.g., Round et al., 2017), and complicate estimations and projections of mass loss (e.g., Arendt et al., 2008; Nuth et al., 2010; King et al., 2021). Glacier surges have been documented at both temperate and polythermal glaciers, where polythermal glaciers are defined as having both cold and temperate ice (Greve and Blatter,

https://doi.org/10.5194/egusphere-2026-913
Preprint. Discussion started: 16 March 2026

2009). Clarke (1976) demonstrates the importance of glacier thermodynamics in regulating the character of polythermal glacier surges, even in cases where peak flow speeds resemble those of temperate glacier surges.

While significant attention has been given to changes in thermal structure (i.e., the spatial configuration of cold and temperate ice) as a mechanism for surge initiation and propagation (e.g., Clarke, 1976; Murray et al., 2000; Fowler et al., 2001; Benn et al., 2019), little work has addressed how surging itself alters long-term glacier thermal structure. Multi-decadal changes in surge character observed in the St. Elias Mountains of the Alaska–Yukon–British Columbia boundary region suggest generally diminishing surge vigour in the form of less extensive surge-related advances (e.g., Eisen et al., 2001; Bevington and Copland, 2014), and in extreme cases, the emergence of "slow surges", where the fast phase of a classical surge fails to materialize altogether (e.g., Frappé and Clarke, 2007; De Paoli and Flowers, 2009). Projected changes in thermal structure under a warming climate include both warming and cooling of glaciers (e.g., Irvine-Fynn et al., 2011; Gilbert et al., 2012; Gusmeroli et al., 2012). Together, past observations (e.g., Sevestre et al., 2015) and future projections (e.g., Wilson and Flowers, 2013) motivate our interest in elucidating the mutual influence of glacier surging and thermal structure in the absence of climate change.

With polythermal glaciers in mind, we seek to determine whether glacier surging alters thermal structure on long (multi-surge) timescales, and whether this could have a feedback on surge character and propensity. We focus on small ($\lesssim$15 km in length) glaciers in this study, as the harbingers of change whose surge cycles and thermal structures are known to be evolving. In approaching this problem from a fundamental as opposed to glacier-specific perspective, we adopt a two-dimensional (flowband) idealized glacier geometry inspired by a real surge-type glacier in Yukon, Canada (Figure 1a & c). We use the thermomechanically coupled ice-flow model `Elmer/Ice` (Gagliardini et al., 2013) to produce a steady-state reference glacier, which we then subject to perturbations of basal friction to produce events of varying magnitude and recurrence interval that resemble surges. By observing the glacier's response to these perturbations and its evolution on various timescales, in the absence of climate variations, we are able to isolate the intrinsic variability that arises from coupled thermomechanical processes.

2 Modeling approach

Below we describe the idealized glacier geometry, the flowband model structure, the numerical model and the surface forcing, followed by the suite of simulations conducted.

2.1 Idealized polythermal glacier

We adopt an idealized glacier geometry reminiscent of an $\sim$8 km long unnamed surge-type glacier (RGI60-01.16732; Clarke et al., 1986; Crompton and Flowers, 2016) which we subsequently refer to as the "reference geometry" (Figure 1a). While the thermal structure of RGI60-01.16732 is unknown, the thermal structure of several similarly sized glaciers in the region has been well established (e.g. Wilson et al., 2013; Clarke and Blake, 1991; Clarke and Goodman, 1975) through a combination of borehole thermometery, englacial radar-scattering measurements and flowband modeling. For example, Wilson et al. (2013) determined the thermal structure of two glaciers within $\sim$20 km of RGI60-01.16732 to be characterized by temperate

https://doi.org/10.5194/egusphere-2026-913
Preprint. Discussion started: 16 March 2026

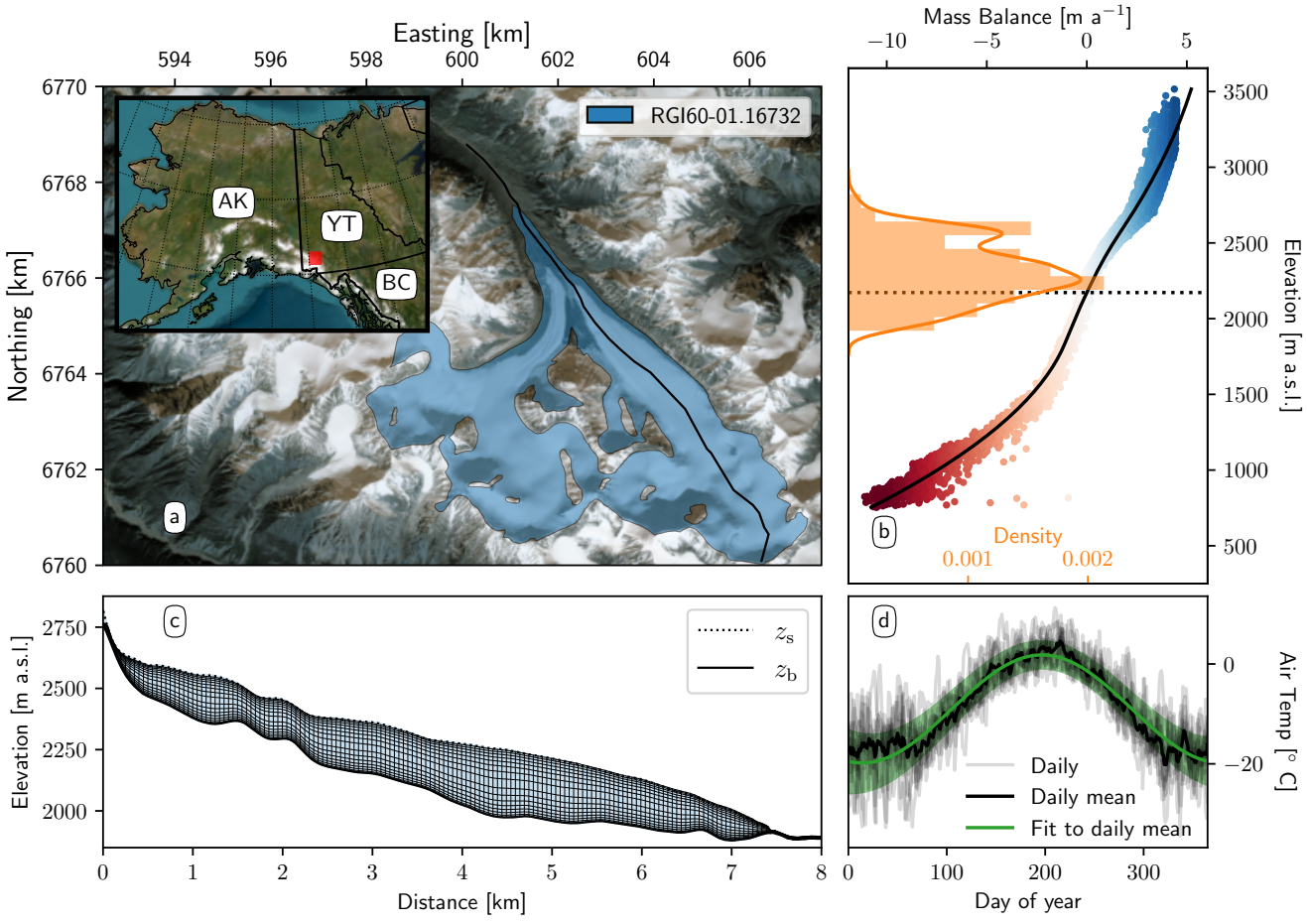

Figure 1. Provenance and characteristics of idealized glacier. (a) Location (red box in inset map) and RGI outline of unnamed glacier (RGI60-01.16732) used to derive idealized geometry and climate. Background image from Sentinel-2, 29 August 2018 (UTM Zone 7N). Base image for the inset map is courtesy of Esri World Imagery. Note: the RGI outline includes two glaciers, but we only use a flowline (black line) along the glacier to the east. (b) Modeled (ice-equivalent) mass balance for zero net-balance conditions ($\mathrm{m\ a^{-1}}$) as a function of elevation for the nearby Kaskawulsh Glacier (∼25 km from RGI60-01.16732 within the red box in (a)) (Robinson et al., 2025). Each point corresponds to a 200 m× 200 m model gridcell. Black line is the quadratic spline used to force the `Elmer/Ice` simulations. Orange line (bars) is the kernel density estimate (normalized histogram) of the area-altitude distribution for the unnamed glacier. (c) Reference glacier flowline geometry created from smoothed surface and bed profiles extracted along flowline shown in (a). (d) Kaskawulsh Glacier-wide average air temperatures derived from downscaled and bias-corrected NARR data, with an applied offset of $-1.3^{\circ}\mathrm{C}$ used to achieve zero net balance. Grey lines are daily glacier-wide average air temperatures for individual years (between 2007–2018). Black line is the daily average of the 12 years. Green line is the non-linear least squares fit of Equation 19 to the daily average temperatures. Shaded green area represents two standard deviations of the daily temperature.

https://doi.org/10.5194/egusphere-2026-913
Preprint. Discussion started: 16 March 2026

accumulation zones and cold ablation zones, where latent heat from meltwater refreezing within the accumulation zone is the dominant heat source.

In the interest of computational efficiency, our modeling approach is restricted to a two-dimensional flowband, where effects of variable flowband width and lateral drag have been neglected (cf. Sergienko, 2012; Gagliardini et al., 2010). We use a TanDEM-X 90m global DEM (Rizzoli et al., 2017) as the source of surface-elevation data and generate a bed DEM from the inferred ice-thickness distributions of Farinotti et al. (2019). Given that these estimates are being used to create idealized profiles to define the reference glacier geometry, realism is important but site-specific accuracy is not. The glacier surface and bed profiles are extracted at 10 m intervals from a manually corrected flowline that avoids right angles and does not cross flow units (Maussion et al., 2019). The resulting surface and bed profiles are smoothed using a fifth order Savitzky-Golay filter with a 210m window (Virtanen et al., 2020). Using the smoothed surface and bed profiles, a structured quadrilateral finite-element mesh is created using the `ElmerGrid` program (Råback, 2023). The mesh has a horizontal spacing of 50 m and 15 vertical layers, which are non-uniformly distributed to achieve higher mesh density at the glacier surface and bed.

2.2 Model description

We model ice flow using `Elmer/Ice` (Gagliardini et al., 2013), which solves the Stokes equations for an incompressible thermoviscous fluid by using a non-linear Glen–Nye constitutive law with $n = 3$ (Greve and Blatter, 2009). We account for the dependence of the creep parameter A ($\mathrm{MPa}^{-3}\ \mathrm{a}^{-1}$) on temperature relative to the pressure melting point T' (K) and water content ω ($-$). Following Aschwanden et al. (2012), energy is conserved through an enthalpy H ($\mathrm{J\ kg}^{-1}$) formulation. Because ice is treated as incompressible, enthalpy is equivalent to internal energy and therefore solely a function of temperature T' (K) and water content ω ($-$) (Aschwanden et al., 2012). We follow Gilbert et al. (2014) and Aschwanden et al. (2012) in ignoring the sensible heat flux in temperate ice and assuming a Fick-type (i.e., diffuse) moisture flux (cf. Darcy-type; Fowler, 1984; Schoof and Hewitt, 2016). The conservation of energy is therefore written:

$$\rho\left(\frac{\partial H}{\partial t} + \boldsymbol{u}\cdot\nabla H\right) = \nabla\left(\kappa\nabla H\right) + Q, \tag{1}$$

where $\boldsymbol{u} = (u, w)$ is the velocity vector ($\mathrm{m\ a}^{-1}$) in the horizontal (x) and vertical (z) directions, Q is a volumetric enthalpy source/sink term ($\mathrm{J\ m}^{-3}\ \mathrm{a}^{-1}$) and κ is the enthalpy diffusivity ($\mathrm{kg\,m}^{-1}\ \mathrm{a}^{-1}$) defined as

$$\kappa = \begin{cases} \kappa_\mathrm{c} = \dfrac{\mathrm{k}(T)}{c(T)}, & H < H_\mathrm{f}(P) \\ \kappa_0 & H \geq H_\mathrm{f}(P) \end{cases}, \tag{2}$$

where $H_\mathrm{f}(P)$ ($\mathrm{J\ kg}^{-1}$) is the enthalpy of fusion as a function of pressure P (MPa), $\mathrm{k}(T)$ is the thermal conductivity ($\mathrm{J\,a}^{-1}\,\mathrm{m}^{-1}\,\mathrm{K}^{-1}$), $c(T)$ is the specific heat capacity ($\mathrm{J\,kg}^{-1}\,\mathrm{K}^{-1}$) of pure ice as function of temperature (Cuffey and Paterson, 2010), κ_c is the enthalpy diffusivity ($\mathrm{kg\,m}^{-1}\,\mathrm{a}^{-1}$) of cold ice and κ_0 is a constant temperate ice diffusivity ($\mathrm{kg\,m}^{-1}\,\mathrm{a}^{-1}$) such that $\kappa_0 \ll \kappa_\mathrm{c}$. Note the difference in units between enthalpy diffusivity ($\mathrm{kg\,m}^{-1}\,\mathrm{a}^{-1}$) and thermal diffusivity ($\mathrm{m}^2\,\mathrm{a}^{-1}$) from classical heat transfer problems (Aschwanden et al., 2012). Following Zwinger et al. (2007) we account for both the temperature $\mathrm{k_i(T)}$ and

https://doi.org/10.5194/egusphere-2026-913
Preprint. Discussion started: 16 March 2026

density dependence $\mathrm{k}_\rho(\rho)$ of thermal conductivity as

$$\mathrm{k}(\rho, \mathrm{T}) = \frac{\mathrm{k}_\rho(\rho)}{\mathrm{k}_\rho(\rho_{\mathrm{ice}})} \mathrm{k}_\mathrm{i}(\mathrm{T}), \tag{3}$$

where ρ_{ice} is the ice density ($\mathrm{kg\,m^{-3}}$; Table X). Within the porous near-surface layer we parameterize the density dependence of the thermal conductivity following Oster and Albert (2022) as

$$\mathrm{k}_\rho(\rho) = 0.144 \exp\left(3.08 \times 10^{-3}\, \rho\right). \tag{4}$$

The thermal conductivity of pure ice $\mathrm{k}_\mathrm{i}(\mathrm{T})$ as a function of temperature (Cuffey and Paterson, 2010) is

$$\mathrm{k}_\mathrm{i}(\mathrm{T}) = 9.828 \exp\left(-5.7 \times 10^{-3} \mathrm{T}\right). \tag{5}$$

2.2.1 Heat sources and sinks

We account for two distinct energy sources ($\mathrm{J\,m^{-3}\,a^{-1}}$) in Eq. (1):

$$Q = \mathrm{tr}\left(\boldsymbol{\sigma}' \dot{\boldsymbol{\varepsilon}}\right) + Q_{\mathrm{lat}}, \tag{6}$$

where the first term represents viscous dissipation (i.e., strain heating), which is the trace tr of the product of the deviatoric stress tensor $\boldsymbol{\sigma}'$ (MPa) and the strain rate tensor $\dot{\boldsymbol{\varepsilon}}$ ($\mathrm{a^{-1}}$), and the second term represents latent heat from meltwater refreezing. Given the units of the terms in the mechanical equations, the viscous dissipation term in Eq. (6) must be scaled by 10^6 $\mathrm{J\,MJ^{-1}}$ to be consistent with the units of Q ($\mathrm{J\,m^{-3}\,a^{-1}}$).

Within the accumulation zone we use a parameterized percolation scheme, similar to that of Gilbert et al. (2012), to prescribe Q_{lat}. For each vertical layer we calculate

$$Q_{\mathrm{lat}} = \begin{cases} \dfrac{r_i L}{\Delta t \Delta z_i} & \text{if } \rho_i \leq \rho_\mathrm{f} \\ 0 & \text{if } \rho_i > \rho_\mathrm{f} \end{cases}, \tag{7}$$

where r_i ($\mathrm{kg\,m^{-2}}$) is the specific mass of meltwater refrozen in the i^{th} layer, Δz_i (m) and ρ_i ($\mathrm{kg\,m^{-3}}$) are the thickness and density of the i^{th} layer, respectively, Δt (a) is the model timestep, L ($\mathrm{J\,kg^{-1}}$) is the latent heat of fusion, and ρ_f ($\mathrm{kg\,m^{-3}}$) is the pore close-off density. The specific mass of refrozen meltwater is calculated as

$$r_i = \min\left(r_{\mathrm{max}}, S_i\right), \tag{8}$$

with S_i ($\mathrm{kg\,m^{-2}}$) the available meltwater in the i^{th} layer and r_{max} ($\mathrm{kg\,m^{-2}}$) the maximum water content that can be accommodated:

$$r_{\mathrm{max}} = \begin{cases} \dfrac{H_\mathrm{f} - H_\mathrm{i}}{L} + \omega_{\mathrm{aq}} \left(1 - \dfrac{\rho_i}{\rho_{\mathrm{ice}}}\right) \rho_\mathrm{w}, & H_\mathrm{i} < H_\mathrm{f} \\ \left(\omega_{\mathrm{aq}} - \omega_\mathrm{i}\right) \left(1 - \dfrac{\rho_i}{\rho_{\mathrm{ice}}}\right) \rho_\mathrm{w}, & H_\mathrm{i} \geq H_\mathrm{f} \end{cases}, \tag{9}$$

https://doi.org/10.5194/egusphere-2026-913
Preprint. Discussion started: 16 March 2026

where H_i and ω_i are the enthalpy and water content of the i^{th} layer, respectively, ω_aq is the maximum water content in the firn column, and ρ_ice and ρ_w are the respective densities of ice and water. The additional term $(H_\mathrm{f} - H_\mathrm{i})/L$ present when $H_\mathrm{i} < H_\mathrm{f}$ represents the refrozen water content required to raise the temperature of the firn to 0°C (i.e., to consume the cold content). The percolation scheme begins at the surface layer ($i = 1$) with

$$S_1 = M\rho_\mathrm{w}, \tag{10}$$

where M (m w.e.) is the surface melt and ρ_w is the density of water. The scheme then iterates over the vertical layers and calculates the liquid water available to the next layer $(i + 1)$ as

$$S_{\mathrm{i}+1} = \max\left(S_\mathrm{i} - r_\mathrm{max}, 0\right). \tag{11}$$

When $r_\mathrm{max} = 0$ (i.e., $\omega = \omega_\mathrm{aq}$) no re-refreezing occurs, as the i^{th} layer cannot accommodate more liquid water. In this case the meltwater represented by S_i percolates to the next vertical layer. Meltwater runoff (m w.e.) is a diagnostic variable in this parameterization (cf. Wilson and Flowers, 2013) and is equal to S_{i+1}/ρ_w once the scheme has iterated over all the vertical layers in the firn column. Within the accumulation zone, we parameterize the near-surface material density $\rho(z)$ (kg m^{-3}) as

$$\rho(z) = \rho_\mathrm{ice} - (\rho_\mathrm{ice} - \rho_\mathrm{s}) \exp\left(-C\left(z_\mathrm{s} - z\right)\right), \tag{12}$$

where C (m^{-1}) is a constant that controls the firn densification rate, ρ_s (kg m^{-3}) is the surface (i.e., snow) density, and z_s (m a.s.l.) is the free surface elevation (Cuffey and Paterson, 2010). By rearranging Eq. (12), we solve for the firn thickness $h_\rho = z_\mathrm{s} - z_\mathrm{f}$ (m), where z_s (m a.s.l.) is the glacier surface elevation and z_f (m a.s.l.) is the elevation where $\rho = \rho_\mathrm{f}$:

$$h_\rho = \frac{1}{C} \ln\left(\frac{\rho_\mathrm{ice} - \rho_\mathrm{s}}{\rho_\mathrm{ice} - \rho_\mathrm{f}}\right), \tag{13}$$

with ρ_f (kg m^{-3}) the pore close-off density.

The surface melt M (m w.e.) used in Eq. (10) is parameterized as

$$M = f_\mathrm{dd}\,\mathrm{PDD}, \tag{14}$$

where f_dd is the degree-day factor for snow (m w.e. K^{-1} d^{-1}) and PDD is the number of positive degree days (K d). Following Calov and Greve (2005) we approximate the number of positive degree days as

$$\mathrm{PDD} = 365 \int_{t_j}^{t_{j+1}} \left[\frac{\sigma(t)}{\sqrt{2\pi}} \exp\left(-\frac{T_\mathrm{s}(t,z)^2}{2\sigma(t)^2}\right) + \frac{T_\mathrm{s}(t,z)}{2} \mathrm{erfc}\left(-\frac{T_\mathrm{s}(t,z)}{\sqrt{2}\sigma(t)}\right)\right] \mathrm{d}t, \tag{15}$$

where t is time (a), t_j and t_{j+1} are the times (a) at the current and next model timestep, respectively, $T_\mathrm{s}(d,z)$ is surface air temperature (K) which depends on the elevation and day of year, $\sigma(d)$ is the standard deviation of the air temperature from the

https://doi.org/10.5194/egusphere-2026-913
Preprint. Discussion started: 16 March 2026

annual cycle (K) which accounts for diurnal variations and further stochastic variations, and erfc is the complementary error function. Note that the integral is scaled by 365 $\mathrm{d\,a^{-1}}$ in order conform with the units of f_{dd} ($\mathrm{m\,w.e.\,K^{-1}\,d^{-1}}$).

Given the poorly constrained nature of water flow within ice (e.g. Fowler and Iverson, 2022; Haseloff et al., 2019; Schoof and Hewitt, 2016), we assume instantaneous drainage once a prescribed threshold water content (ω) is reached (e.g. Gilbert et al., 2014; Gilbert et al., 2020). We adopt different thresholds for the porous near-surface layer ($\omega_{\max_{\mathrm{aq}}}$) and the englacial environment ($\omega_{\max_{\mathrm{en}}}$), where $\omega_{\max_{\mathrm{en}}} < \omega_{\max_{\mathrm{aq}}}$ (Table 2).

2.2.2 Kinematic boundary condition

For the time-dependent (i.e., prognostic) simulations we solve the free surface equation

$$\frac{\partial z_{\mathrm{s}}}{\partial t} + u_{\mathrm{s}}\frac{\partial z_{\mathrm{s}}}{\partial x} - w_{\mathrm{s}} = \dot{b}, \tag{16}$$

where z_{s} is the glacier surface elevation, $(u_{\mathrm{s}}, w_{\mathrm{s}})$ are the surface velocities obtained from the dynamic governing equations and $\dot{b} = \dot{b}(x,t)$ is the surface mass balance (accumulation minus ablation). We assume rigid, impermeable bedrock of elevation $z_{\mathrm{b}}(x)$, thus Eq. (16) must satisfy the inequality

$$z_{\mathrm{s}}(x,t) \geq z_{\mathrm{b}}(x) + h_{\min} \;\; \forall\, x,t, \tag{17}$$

where $h_{\min}$ (m) is a small positive ice thickness ($h_{\min} = 10\,\mathrm{m}$) used to ease the numerical solution of Eq. (16), which is a free boundary problem subject to the variational inequality (Eq. 17) (Gagliardini et al., 2013).

2.2.3 Surface boundary conditions

We impose a stress-free condition at the free surface (Greve and Blatter, 2009, pg. 67) and prescribe a Dirichlet condition for Eq. (1):

$$H_{\mathrm{s}} = H\left(\max\left(T_{\mathrm{s}}(t,z), 273.15\right)\right), \tag{18}$$

where the surface temperature is defined by:

$$T_{\mathrm{s}}(t,z) = T_{\mathrm{ma}} + \alpha\cos\left(2\pi\left(t - \frac{T_{\mathrm{p}}}{365}\right)\right) + (z - z_{\mathrm{ref}})\frac{\partial T}{\partial z}, \tag{19}$$

with T_{ma} the mean annual air temperature (K) at reference elevation z_{ref} (m), α the amplitude of the annual air temperature cycle (K), T_{p} the day of year (d.o.y.) of the air-temperature maximum (d) and $\frac{\partial T}{\partial z}$ the atmospheric lapse rate ($\mathrm{K\,m^{-1}}$).

2.2.4 Basal boundary conditions

We use a linear Weertman-type sliding law to relate the basal shear stress τ_{b} (MPa) to the basal sliding velocity $\boldsymbol{u}_{\mathrm{b}}$ ($\mathrm{m\,a^{-1}}$):

$$\boldsymbol{u}_{\mathrm{b}}(H) = \begin{cases} 0, & H < H_{\mathrm{f}} \\ \beta^2\tau_{\mathrm{b}}, & H \geq H_{\mathrm{f}} \end{cases}, \tag{20}$$

https://doi.org/10.5194/egusphere-2026-913
Preprint. Discussion started: 16 March 2026

where β^2 is the basal drag coefficient ($\mathrm{m\ a^{-1}MPa^{-1}}$). Eq. 20 only permits sliding where the bed is temperate (at the pressure melting point).

The basal boundary condition on enthalpy (Eq. 1) is dependent on the thermal state of the ice–bed interface $z = z_\mathrm{b}$. In the case of cold ice ($H < H_\mathrm{f}(P)$) we prescribe a Neumann condition:

$$(\nabla H \cdot \boldsymbol{n}_\mathrm{b})|_{z=z_\mathrm{b}} = -Q_\mathrm{geo}\frac{c}{\mathrm{k_i}}, \tag{21}$$

where Q_geo is the geothermal heat flux ($\mathrm{J\,a^{-1}\,m^{-2}}$) and $\boldsymbol{n}_\mathrm{b}$ is the (outward-pointing) unit vector normal to the bedrock. If the ice–bed interface is temperate, but there is no overlying temperate ice, we prescribe a Dirichlet condition:

$$H|_{z=z_\mathrm{b}} = H_\mathrm{f}(P). \tag{22}$$

In the case that the ice–bed interface is temperate and overlain by a finite thickness of temperate ice, we follow Aschwanden et al. (2012) in prescribing an insulating Neumann condition:

$$(\nabla H \cdot \boldsymbol{n}_\mathrm{b})|_{z=z_\mathrm{b}} = 0. \tag{23}$$

We do not account for mass lost/gained through basal melt/freeze-on (i.e., non-zero basal mass balance), leading to small violations of mass conservation. For a representative simulation with widespread fast sliding as described below, we find a maximum basal melt rate of $\sim 8\ \mathrm{cm\ a^{-1}}$. Such values are spatially localized in topographic depressions and arise from the use of the unbounded (linear) sliding law (Equation 20). Even if basal melt rates are overestimated in the model, they still present $< 0.01\%$ violation of the conservation of mass over the span of a surge.

2.3 Surface Forcing

We use air-temperature data and surface mass-balance estimates from the nearby Kaskawulsh Glacier produced by Robinson et al. (2025) as the surface forcing in our simulations. Surface mass balance is used to drive the dynamics (Eq. 16) and air temperature is used to prescribe surface boundary conditions for the thermodynamics (Eq. 18) and to calculate the latent heat from meltwater refreezing (Eq. 7–15). It is important to note that the surface melt (Eq. 14) calculated as part of the meltwater percolation scheme is not coupled to the surface mass balance estimates used to drive the dynamics.

2.3.1 Surface mass balance

The surface mass balance estimates used in this study, produced by Robinson et al. (2025), employ the mass-balance model of Young et al. (2021), an enhanced temperature-index melt model (Hock, 1999) driven by downscaled and bias-corrected North American Regional Reanalysis (NARR) 2-m air-temperature and precipitation data with model parameters tuned by for the Kaskawulsh Glacier using the glacier-wide 2007–2018 geodetic balance, the average equilibrium line altitude (ELA) and in-situ mass-balance data. The geodetic balance of the Kaskawulsh Glacier has been negative and closely follows the regional average over several decades (Berthier et al., 2010), suggesting that this glacier is representative of the larger region (including our area of interest $\sim$25 km away). To drive simulations of the reference glacier geometry, we create a new field corresponding

https://doi.org/10.5194/egusphere-2026-913
Preprint. Discussion started: 16 March 2026

to conditions of zero net balance for the Kaskawulsh Glacier by re-running the mass-balance model with air temperatures shifted by a constant offset. We then use a second-order spline $\mathcal{S}(z)$ ($\mathrm{m\,a^{-1}}$; black line in Figure 1b) to describe mass balance as a function of elevation for these zero net-balance conditions, and use this function to drive the simulations described below.

2.3.2 Air temperature

We use the shifted air temperatures to compute the mean daily air temperature over a seasonal cycle at 2193 $\mathrm{m\,a.s.l.}$ (mean surface elevation of the Kaskawulsh Glacier, hereafter the reference elevation z_{ref} in Eq. 19). We then use a non-linear least squares fitting routine (`curve_fit` from `scipy.optimize`, Virtanen et al., 2020) to fit the air-temperature parameterization (Eq. 19) to the air-temperature timeseries in Figure 1d. Figure 1d demonstrates the seasonal dependence of daily air-temperature variability as captured in the standard deviation, with greater variability in winter than summer. Therefore, we also fit a second-order polynomial to the standard deviation of air temperature as a function of time, and use this time-dependent standard deviation $\sigma(t)$ in the calculation of positive degree days (PDDs) (Eq. 15) for the latent heat source parameterization (Eq. 7).

2.3.3 Initialization and sensitivity tests

Using the reference geometry described above (§2.1), we now determine steady-state configurations as a function of air temperature and mass balance, with the goal of defining a single "reference glacier" to be used as the initial condition for the surging experiments described below. While the glacier that inspired the reference geometry is not in steady state (e.g., Berthier et al., 2010), we have chosen a steady-state initialization for simplicity, and we test a range of surface forcings to assess the sensitivity of steady-state thermal structure to these forcings. For $\mathcal{S}(z)$ the second-order spline ($\mathrm{m\,a^{-1}}$) in Figure 1b, the initialization simulations use

$$\dot{b}(z) = \mathcal{S}(z) + \Delta\dot{b}, \tag{24a}$$

$$\hat{T}_{\mathrm{ma}} = T_{\mathrm{ma}} + \Delta T, \tag{24b}$$

where $\Delta\dot{b}$ is a prescribed mass-balance anomaly and $\dot{b}$ is used in Eq. (16), ΔT is a prescribed air-temperature anomaly, and $\hat{T}_{\mathrm{ma}}$ is the perturbed mean annual air temperature at z_{ref}, which is used instead of T_{ma} in Eq. (19). As part of the initialization experiment we conduct a grid search across plausible values of the mean annual air-temperature anomaly ΔT and the mass-balance anomaly $\Delta\dot{b}$. We define two parameter sets:

$$\begin{aligned} \mathcal{T} &= \{0.0,\, 0.1,\, \ldots,\, 0.9,\, 1.0\} \\ \mathcal{B} &= \{-0.25, -0.26, \ldots, -0.49, -0.50\}, \end{aligned} \tag{25}$$

where $\mathcal{T}$ is a 11-element set of mean annual air-temperatures anomalies (ΔT) and $\mathcal{B}$ is an 26-element set of mass-balance anomalies ($\Delta\dot{b}$). The grid search is defined by parameter combinations

$$\mathcal{B} \times \mathcal{T} = \{(\Delta T, \Delta\dot{b}) \,|\, \Delta T \in \mathcal{T} \text{ and } \Delta\dot{b} \in \mathcal{B}\}, \tag{26}$$

https://doi.org/10.5194/egusphere-2026-913
Preprint. Discussion started: 16 March 2026

where $\times$ is the Cartesian product, and $\mathcal{B} \times \mathcal{T}$ is a 286-element set of parameter values. All possible combinations of ΔT and $\Delta \dot{b}$ are tested in order to thoroughly assess model sensitivity to climatic forcing.

To select a reference model from the simulations above, we first discard all simulations that produce a difference between the initial and steady state glacier volumes greater than 1% (i.e., outside $V' = 1.00 \pm 0.01$, dotted black contours in Figure 2a). From the remaining simulations, we aim to select the one situated in the region of $\Delta \dot{b}$–ΔT space most representative of the study area that inspired this work. To do this we empirically estimate a relationship between $\Delta \dot{b}$ and ΔT. True perturbations to mass balance (i.e., $\Delta \dot{b}$) occur via changes in accumulation and ablation which are largely driven by air temperature and precipitation, but may also involve variables such as cloud cover, wind speed, and humidity (Eq. 4.8; pg 106 Cuffey and Paterson, 2010). Under the simplifying assumption that mass-balance anomalies $\Delta \dot{b}$ are dominantly driven by temperature anomalies ΔT, we write

$$\Delta \dot{b} = \left(\frac{\partial \dot{b}}{\partial T} \right) \Delta T, \tag{27}$$

where $\frac{\partial \dot{b}}{\partial T}$ ($\mathrm{m\ a^{-1}\ K^{-1}}$) is the mass-balance sensitivity, which we estimate using the mass-balance model output of Robinson et al. (2025). Neglecting any spatial dependence of the mass-balance sensitivity, we estimate $\frac{\partial \dot{b}}{\partial T} = -0.764\ \mathrm{m\ a^{-1}\ K^{-1}}$. Equation 27 defines the equation of a line through $\Delta \dot{b}$–ΔT space (solid white line in Figure 2). We define the reference model as the simulation within the target volume envelope closest to this line.

Once the reference glacier has been identified, we quantify its sensitivity to numerical and parametric choices in the thermodynamic component of the model. We test the sensitivity to four model parameters: the degree-day factor f_{dd} ($\mathrm{m\ w.e.\ K^{-1}\ d^{-1}}$), firn column thickness h_ρ (m), maximum englacial water content ω_{en} ($\%$), and maximum firn aquifer water content ω_{aq} ($\%$). We also test the sensitivity to the enthalpy initial condition and the number of vertical layers in the mesh. Because prognostic simulations are computationally expensive (cf., diagnostic simulations), we use the one-at-a-time method where each parameter or model choice is varied independently to limit the total number of simulations (cf., Aschwanden et al., 2019; Hill et al., 2021). Reference parameter values and the parameter ranges tested are listed in Table 2. The ranges are meant to span physically plausible values, even if not representative of the study region (Figure 1). Parameter sampling is refined where needed to resolve the model sensitivity (Nolan, 2023).

Initialization simulations and sensitivity tests are run for 3 ka, with a timestep Δt_{D} of 1 a for ice dynamics (i.e., mechanical equations: S2, S4, & 16) and a timestep Δt_{T} of 0.1 a for thermodynamics (Eq. 1). The thermodynamic equation uses a smaller timestep to ensure adequate sampling of the seasonal cycle in the air-temperature forcing (Figure 1d). The mechanical equations use a larger timestep to maximize computational efficiency, since the `Navier-Stokes` solver is the most computationally expensive solver used. All simulations start at $t = 0$ with isothermal (temperate) initial conditions, except for sensitivity tests where the initial conditions are varied. For the initialization experiments, we enforce a no-slip boundary condition (i.e. $\beta^2 = 1$) at the glacier bed, such that $u_{\mathrm{b}}(x, z) = 0$.

https://doi.org/10.5194/egusphere-2026-913
Preprint. Discussion started: 16 March 2026

2.3.4 Forced surges

Using the reference glacier from the initialization experiments, we conduct idealized numerical experiments to understand the mutual influence of glacier surging and thermal structure in a stationary climate. As modeling of surge initiation (e.g., Minchew and Meyer, 2020) and propagation (e.g., Thøgersen et al., 2019) are active areas of research, we merely attempt to emulate the effects of surging by prescribing surge-like perturbations to basal traction as in Morin et al. (2023).

In the first set of surging experiments, a two-year surge-like perturbation (henceforth referred to simply as a "surge" for brevity) is imposed, as one to two years represents a typical duration of the fast phase of a surge in the St. Elias Mountains (e.g., Meier and Post, 1969; Murray et al., 2003; Sevestre and Benn, 2015). Surge vigor is varied by using nine logarithmically spaced values of the basal slip coefficient (β^2) ranging from 10^{-3} to 10^{-4} $\mathrm{m\ a^{-1}\,MPa^{-1}}$. Sliding can only occur where the ice–bed interface is at the pressure melting point (Eq. 20). We further restrict sliding to $z_\mathrm{b} \leq$2400 m a.s.l. to inhibit excessive drawdown in the steepest highest region of the accumulation zone. Following the surge, sliding is set to zero during a 4 ka quiescent period. This sequence of a 2 a surge and a 4 ka quiescence is then repeated a second time, for a total simulation time of 8004 a. Because the initial condition represents a steady state with respect to the climate forcing (e.g., Figure S1a & c), which is never the case for surge-type glaciers (Meier and Post, 1969; Sevestre and Benn, 2015), the purpose of this experiment is two-fold: (1) to understand how a single surge event alters thermal structure independent of climate and (2) to quantify the thermodynamic recovery timescale following a surge.

In the second suite of surging simulations we force 2 a surges with recurrence intervals T_s of 15, 30 and 60 a irrespective of whether the glacier geometry has recovered between surges. Simulations are run for 9 ka and use the recovered steady-state configurations (§2.3.3) as the initial condition. Simulation results are compared to the initial condition, which we take as representative of a non-surge-type glacier, in order to characterize the effects of surging. As in the previous experiment, we restrict sliding to $z_\mathrm{b} \leq$ 2400 m a.s.l.. In this case we used 30 logarithmically spaced values of β^2 from $1\mathrm{e}^{-3}$ to $1\mathrm{e}^{-4}$ $\mathrm{m\,a^{-1}\,MPa^{-1}}$. For all surging experiments, the ice-dynamics timestep (Δt_D) and thermodynamics timestep (Δt_T) are both set to 0.05 a during the surge, whereas $\Delta t_\mathrm{D} = 1$ a and $\Delta t_\mathrm{T} = 0.1$ a during quiescence.

2.4 Simulation strategy

Five diagnostic scalar metrics are computed for each simulation to allow for quantitative comparison between simulations with different surface forcings and/or prescribed surge characteristics: glacier volume per unit width V' (−), length L (km), fraction temperate FT (−), fraction temperate bed FT_b (−) and mean enthalpy $\bar{H}$ (J $\mathrm{kg^{-1}}$). These metrics and their temporal evolution are also used to determine whether a given simulation has reached a (dynamic) steady state. More information about these scalar metrics and how they are calculated can be found in §S2 of the supplementary material.

https://doi.org/10.5194/egusphere-2026-913
Preprint. Discussion started: 16 March 2026

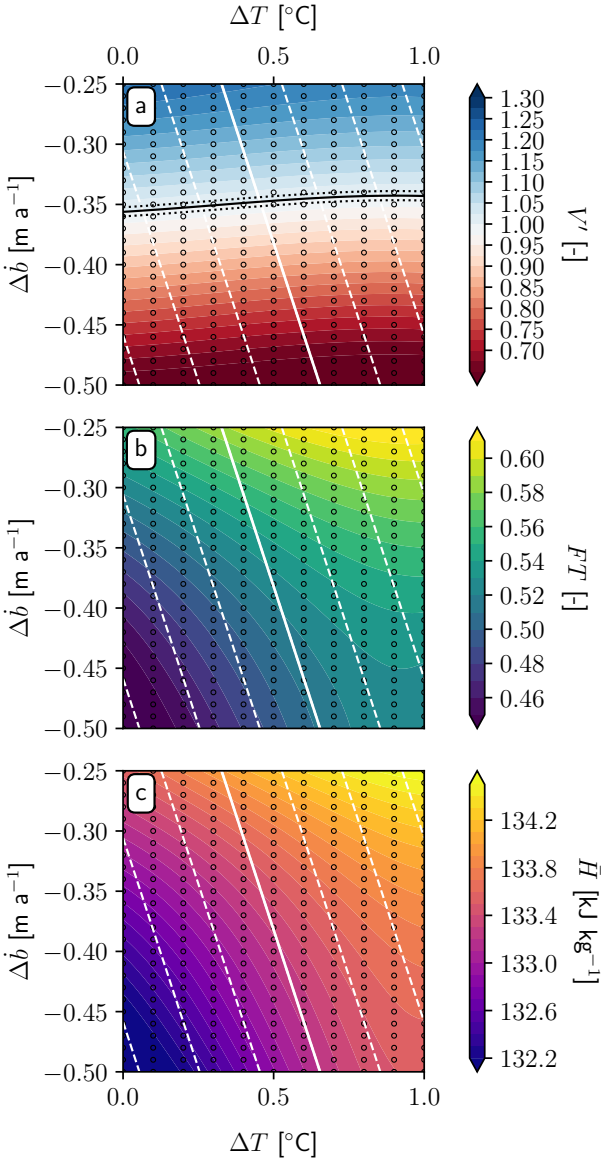

Figure 2. (a) Relative volume per unit width V' (−), (b) fraction temperate FT (−), and (c) mean enthalpy $\bar{H}$ (kJ kg^{-1}) at the end of the 3 ka initialization simulations. (a) Solid black horizontal line is the $V' = 1$ contour, dotted black lines are $V' = 1 \pm 0.01$ contours. (a-c) Dashed white lines represent plausible $\hat{T}_{\mathrm{ma}}$–$\Delta\dot{b}$ relationships for arbitrary T_{ma} assuming constant $\frac{\partial \dot{b}}{\partial T}$. Solid white line is the relationship that corresponds to T_{ma} from Table X. Black circles indicate simulations run as part of initialization the grid search (Eq. 25).

https://doi.org/10.5194/egusphere-2026-913
Preprint. Discussion started: 16 March 2026

3 Results: initialization and sensitivity tests

3.1 Initialization

Across the $0.25\,\mathrm{m\,a^{-1}}$ variations in $\Delta\dot{b}$ and $1\,^{\circ}\mathrm{C}$ variations in ΔT, all 286 simulations produce the same general thermal structure (Figure 3), which is characterized by a cold ablation zone and a mostly temperate accumulation zone with water content at or near the maximum value (ω_{en}=1%). At the lowest values of ΔT, surface melt is sufficiently restricted that cold ice is produced along the headwalls and advected to the central accumulation zone, thereby bisecting the temperate ice produced by meltwater refreezing at the surface and strain heating along the ice–bed interface ($\Delta T = 0.0\,^{\circ}\mathrm{C}$ in Figure 3).

The mass-balance anomaly is the primary control on steady-state glacier volume, while the mean annual air temperature only exerts a minor control (Figure 2a, S1a,b vs. S1c,d). A $0.25\,\mathrm{m\,a^{-1}}$ change in $\Delta\dot{b}$ produces an average change of 60% in V', while a $1\,^{\circ}\mathrm{C}$ change in ΔT produces an average change of only 4 % in V'. Most of the change in V' with ΔT occurs over the lower values of ΔT ($< -0.4,^{\circ}\mathrm{C}$), where surface melt is sufficiently restricted and cold ice is produced in the upper accumulation zones (Figure 3). Despite the 60% variation in glacier volume across the grid search, nearly all glaciers reach a steady state, defined by $< 1\%$ change in $V'(t)$ over the last $500\,\mathrm{a}$ of the initialization simulation (e.g. Figure S1a & c). The eight glaciers that do not meet this criteria have steady-state terminus positions that lie on retrograde bed slopes (shaded red region Figure S1b & d). The maximum change in $V'(t)$ for all 286 simulations over the last $500\,\mathrm{a}$ is 1.16%.

The mass-balance anomaly $\Delta\dot{b}$ again is an important control on all three thermodynamic metrics (Figure 2), while ΔT exerts little influence over glacier volume (Figure 2a). While changes in $\Delta\dot{b}$ do significantly alter the thermodynamic metrics, it is important to note that only changes in ΔT alter the thermal structure itself (Figure 3). For a fixed value of ΔT, the changes in the thermodynamic metrics with $\Delta\dot{b}$ occur for two reasons. First, as the ELA lowers (via less negative $\Delta\dot{b}$ values) the area over which latent heat (Q_{lat}) is produced increases, meaning more temperate ice is created. Second, with less negative $\Delta\dot{b}$ values, the glaciers become longer (Figure S1b) and, more importantly, thicker (Figure S1b), meaning advection rates increase. Less negative values of $\Delta\dot{b}$ therefore produce more temperate ice and higher advection rates, which serve to transfer temperate ice more efficiently down-glacier. The combined effect of a stronger heat pump and greater advection rates means FT and $\bar{H}$ all increase with increasing mass balance (Figures 2 a, 2b, 2b). The changes in thermal structure (and therefore the thermodynamic metrics) with ΔT primarily occur due to the restriction of surface melt over the upper reaches of the accumulation zone.

3.2 Reference glacier

Using the change in relative volume and perturbed air temperature criteria outlined in §2.3.3, we identify a reference glacier as the grid search member initialized with $\Delta T = -0.5\,^{\circ}\mathrm{C}$ and $\Delta\dot{b} = -0.36\,\mathrm{m\,y^{-1}}$ (Figure S2). The reference glacier has mean and maximum ice thicknesses of $122\,\mathrm{m}$ and $236\,\mathrm{m}$, respectively. The ELA is $2273\,\mathrm{m\,a.s.l.}$, resulting in an accumulation area ratio of 0.4. Surface melt (Eq. 14) occurs over the entire accumulation zone but meltwater runoff only occurs over the lower half of the accumulation zone, meaning the firn aquifer in the lower half of the accumulation zone is saturated. Like all glaciers in the grid search described above, the reference glacier has a temperate accumulation zone and cold ablation zone (Figure 3), with a small amount of cold ice formed on the headwall (Figure S2a). A seasonally variable layer forms in the ablation zone,

https://doi.org/10.5194/egusphere-2026-913
Preprint. Discussion started: 16 March 2026

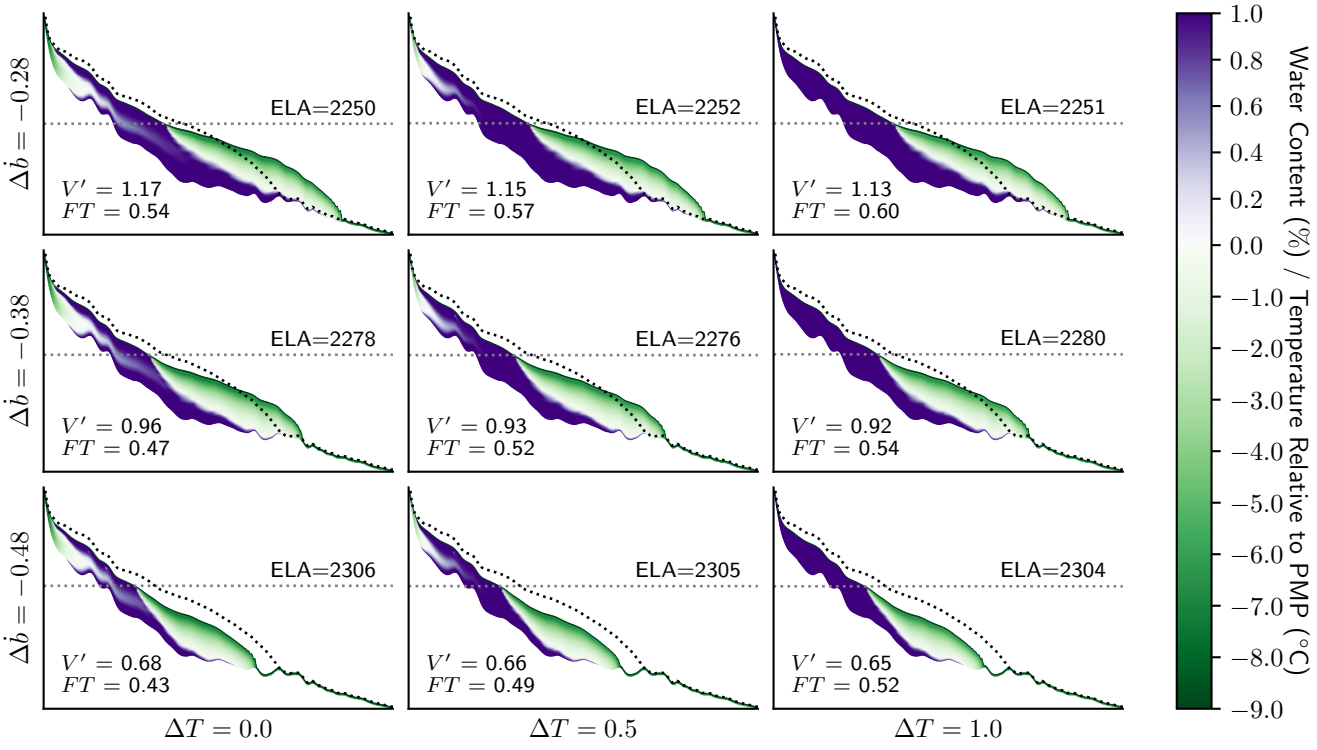

Figure 3. Subset of steady-state thermal structures at 3 ka from the surface-forcing grid search. Purple is water content (i.e., temperate ice) and green is temperature relative to the pressure melting point (PMP; i.e., cold ice). Rows are different mass balance anomalies $\Delta\dot{b}$ ($\mathrm{m\,a^{-1}}$) and columns are different mean annual air temperatures ΔT (°C) at z_{ref}. Dotted black line is the initial profile. Fraction temperate FT $(-)$ and relative volume per unit width V' $(-)$ at 3 ka are reported in the bottom left of each subplot.

but does not alter the thermal structure more than $\sim 25\,\mathrm{m}$ below the free surface. Maximum speed is $\sim 25\,\mathrm{m\,y^{-1}}$ 1.5–2.5 km along the flowline from the headwall (Figure S2b). This area also corresponds to the area of maximum Péclet number (Figure 3c). Energy transport in the temperate ice is advection dominated ($\mathrm{Pe} \gg 1$) owing to the low diffusivity of temperate ice, while energy transport in the cold ice is diffusion dominated ($\mathrm{Pe} < 1$). Pe is discontinuous along the cold–temperate transition surface (CTS), due to the discontinuity in κ (Eq. 2). $\mathrm{Pe} = 0$ along the ice-bed interface, even in the temperate ice regions, due to the no-slip (i.e. $u_{\mathrm{b}} = 0$) boundary condition (Figure S2c).

3.3 Sensitivity tests

Parameters that limit the amount of meltwater refreezing (i.e. latent heat production) in the firn aquifer have the strongest effect on our model results (Figure S3), consistent with the work of Wilson and Flowers (2013). As latent heat production decreases, glaciers become colder and larger in our simulations (Figure S3). Since the degree day factor (f_{dd}) and the firn aquifer thickness (h_ρ) have the greatest ability to limit latent heat production, with the former reducing the amount of surface

https://doi.org/10.5194/egusphere-2026-913
Preprint. Discussion started: 16 March 2026

melt available for refreezing and the latter reducing the amount of refrozen meltwater that can be accommodated by firn aquifer (Figure S3i & ii), our model is most sensitive to reductions in these parameters. The maximum englacial water content (ω_{en}), which alter ice flux through the ω-dependent ice-flow enhancement factor (Eq. S18), results in a (nearly) linear change in FT, $\bar{H}$, and V' across the seven values tested. Across the nine values tested, the maximum firn aquifer water content (ω_{aq}) has a negligible effect on the steady-state configuration of the reference glacier. For more information about the reference glacier's sensitivity to each of the parameters tested, see Nolan (2023).

The initial condition for enthalpy has no effect on the steady-state configuration of the reference glacier (V', FT, $\bar{H}$) across the $10^{\circ}\mathrm{C}$ range tested. While the initial condition does not alter the steady-state configuration, it does alter the time required to reach steady state, with lower temperatures requiring longer. A doubling of number of vertical mesh layers (N_{z}) from 15 to 30 results in $< 0.5\%$ difference in V'. The two meshes converge to the same values of FT, but the $N_{\mathrm{z}} = 30$ mesh has a slightly smaller seasonal envelope in FT. The finer mesh more accurately resolves the seasonal layer, resulting in small differences in mean enthalpy ($< 2\ \mathrm{kJ\,kg^{-1}\,K^{-1}}$). These small differences in enthalpy are confined to the near-surface and do not alter the steady-state configuration significantly.

4 Results: forced surges

4.1 Steady-state recovery after a single surge

Following the surges, all simulations irrespective of surge vigor (i.e., set by the value of β^2) converge to the same configuration, which is slightly ($\sim 1.25\%$) smaller in volume (V') than the reference glacier (Figure 4a). The recovered values of fraction temperate (FT) and mean enthalpy ($\bar{H}$) are X and X $\%$ larger, respectively (Figure 4b,c). The time to reach these recovered steady states increases with increasing surge vigor (i.e., decreasing β^2) and is about $\sim$2.25 times longer for V' (2425 a) as compared to FT and $\bar{H}$ (1084 a) (Figure 4). The longer timescales for dynamics variables (e.g., V') to reach steady state than thermodynamics variables (e.g. FT, $\bar{H}$) are consistent with results from the initialization experiments and expectation (Cuffey and Paterson, 2010). The recovery timescales are much longer than typical surge-recurrence intervals, suggesting that polythermal surge-type glaciers in the St. Elias Mountains do not achieve a thermodynamic steady state between surge events (e.g., Wilson et al., 2013). The recovery timescales shown in Figure 4 should be considered an upper bound, as we do not include crevassing in our model which should shorten the thermodynamic response time (Gilbert et al., 2020).

Analogous experiments with an isothermal temperate version of the reference geometry produce similar magnitude differences in relative volume as the thermomechanically coupled experiments (compare Figure S4 and Figure 4a). Given the consistent differences in V' between the thermomechanically coupled and isothermal simulations and the consistent recovered configuration despite changes in β^2, we suggest the small differences in recovered relative volume are due to mass-balance–elevation feedbacks, rather than thermodynamic effects. We caution against over-interpretation of the small differences in recovery values of FT and $\bar{H}$ relative to their reference values (Figure 4b,c): the prescribed constant firn-column thickness above the ELA (Eqn. 12) is too simplistic to resolve the elevation-dependent feedbacks that would have the potential to alter the recovery values. Specifically, changes in accumulation, and therefore firn-column thickness, as a function of surface elevation

https://doi.org/10.5194/egusphere-2026-913
Preprint. Discussion started: 16 March 2026

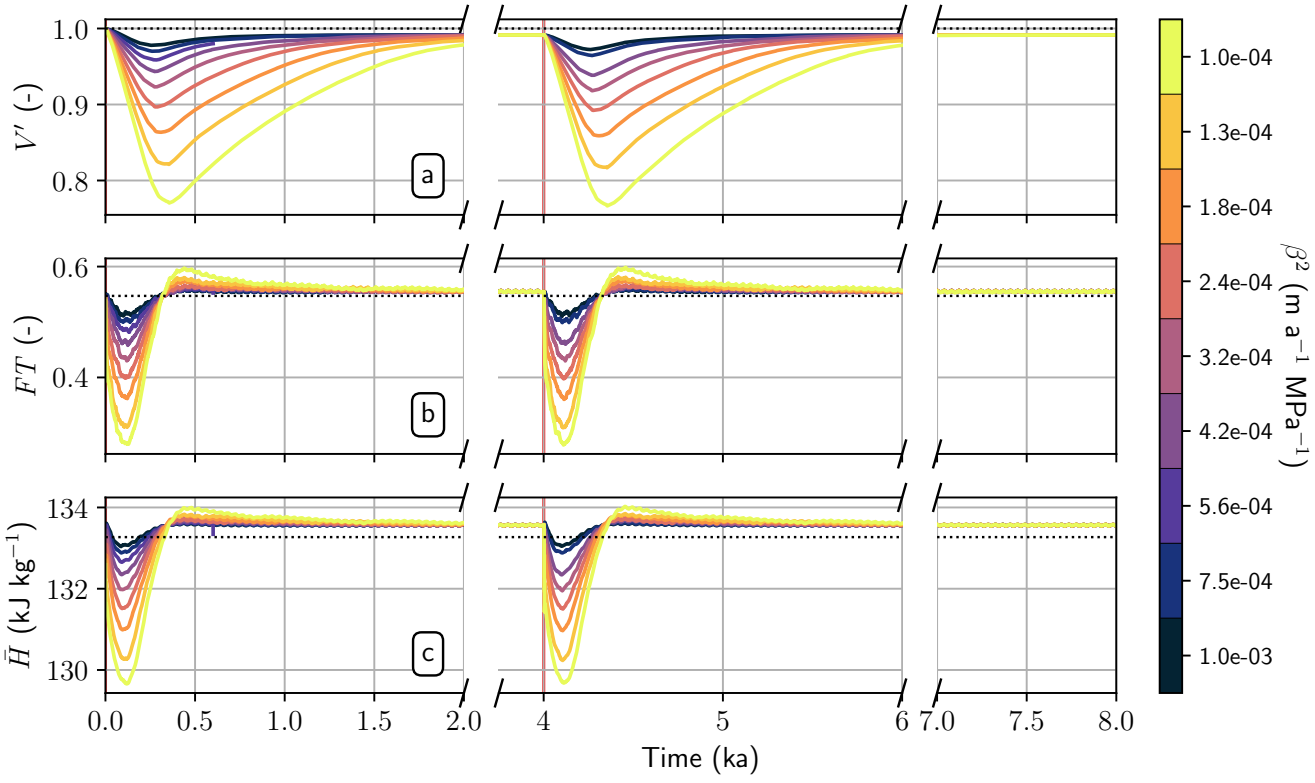

Figure 4. Recovery following two-year surges at 0 and 4 ka (vertical pink line). (a) Relative volume per unit width V'. (b) Fraction temperate FT. (c) Mean enthalpy $\bar{H}$ (kJ kg^{-1} K^{-1}). Dotted black lines denote the steady-state (i.e., pre-surge) values of the reference glacier. The time axis is broken between 2–3.75 ka and 6–7 ka for better visualization of transient responses.

are not explicitly resolved in our model. While the surges do not alter the recovered thermodynamic configuration in the model, we cannot exclude this possibility with a more physically realistic representation of surface processes.

4.2 Periodic surges

Surging results in smaller (Figure 5a) and colder (Figure 5b and c) glaciers relative to the initial condition. Surging has previously been shown to alter glacier mass balance and therefore volume (Adalgeirsdóttir et al., 2005), but here we further demonstrate that glaciers become smaller with increasing surge magnitude (decreasing β^2 in Figure 5a). Surges alter mass balance by transporting mass from the reservoir zone to the receiving zone where ablation rates are higher; over the cycle of multiple surge events the increased ablation results in a smaller glacier volume when subject to the same surface forcing (Adalgeirsdóttir et al., 2005). As the magnitude of the surge increases, the amount of mass transported to lower elevations increases, resulting in smaller, thinner glaciers (Figure 5a). These glaciers have lower advection rates, meaning a reduced flux of temperate ice down glacier and higher rates of conductive cooling (i.e., vertical diffusion), resulting in colder glaciers over-

https://doi.org/10.5194/egusphere-2026-913
Preprint. Discussion started: 16 March 2026

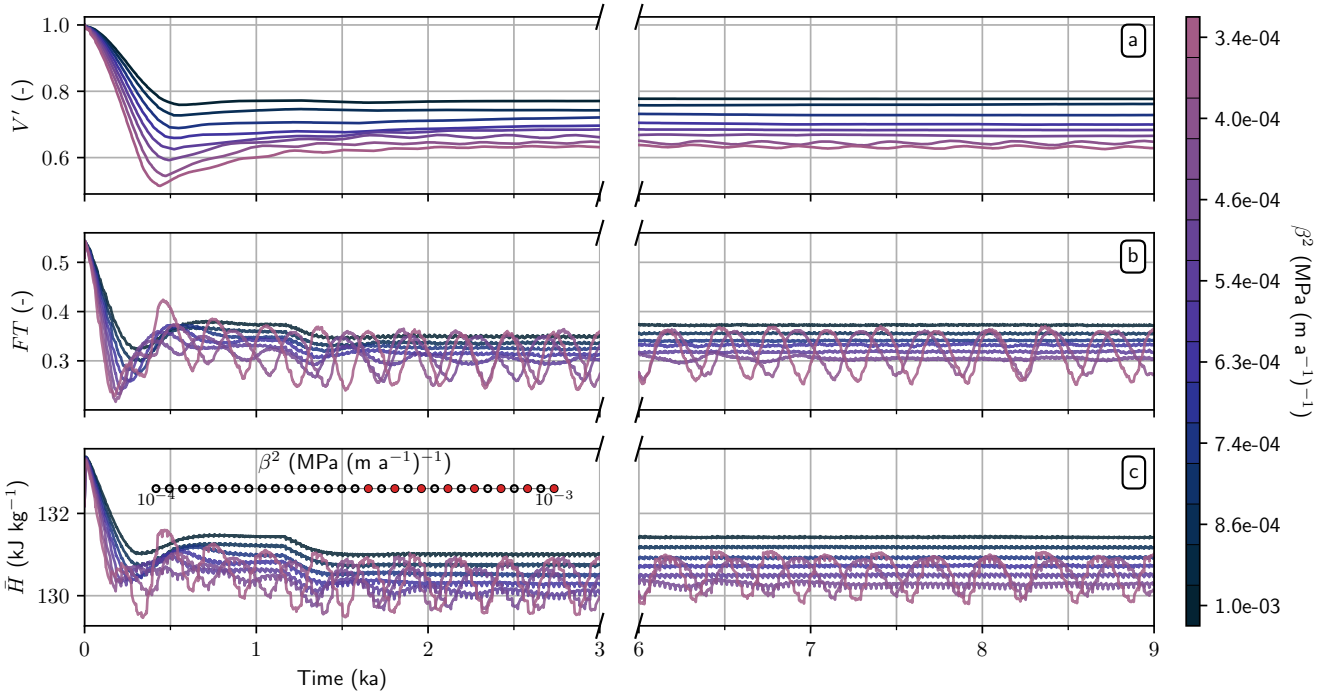

Figure 5. Transient response to prescribed periodic surge events with a surge cycle (T_s) of 30 a for eight values of β^2 (colors). Decreasing values of β^2 correspond to greater rates of basal sliding (Equation 20). Note the break in the x axis from 3–6 ka. (a) Relative volume per unit width V'. (b) Fraction temperate FT. (c) Mean enthalpy $\bar{H}$ (kJ kg^{-1} K^{-1}). Grey on the logarithmic number line in (c) denote the full suite of β^2 values sampled, while red markers denote the simulations plotted here. Low amplitude, high frequency oscillations in FT (b) and $\bar{H}$ (c) correspond to prescribed surges, while high amplitude, low frequency oscillations for $\beta^2 \leq 4.6 \times 10^{-4}$m a^{-1} MPa^{-1} are unforced. Only a subset of β^2 values are plotted to highlight the emergence of the unforced oscillation.

all (Figure 5b & c). The effects described above could be even more pronounced with a model that accounted for crevassing, where surface-area increase from crevassing may lead to greater ablation and cooling (cf. Gilbert et al., 2020).

For surge events with a 30-a return interval (Figure 5), the relationship between glacier volume/thermal structure and surge vigor (as controlled by β^2) is simple until $\beta^2 \leq 4.6 \times 10^{-4}$ m a^{-1} MPa^{-1} , whereupon an unforced low frequency ($\approx \frac{1}{300}$ a^{-1}) oscillation emerges in all three time series (V', FT, $\bar{H}$) shown in Figure 5. To examine the mechanism by which these unforced oscillations arise we examine the representative case of $\beta^2 = 3.16 \times 10^{-4}$ m a^{-1} MPa^{-1} in more detail.

4.2.1 Oscillation mechanism

Figure 6 (a–d) shows timeseries of fraction temperate FT (−), fraction temperate bed FT_b (−), ice thickness at the ELA h_{ELA} (m), and average surface speed $|\bar{\boldsymbol{u}}|$ (m a^{-1}), from 7.5–9.0 ka for $\beta^2 = 3.16 \times 10^{-4}$ m a^{-1} MPa^{-1} and $T_s = 30$ a. Figure 6 (e–g) shows snapshots of the longitudinal strain rate $\dot{\varepsilon}_{xx}$ (a^{-1}; Figure 6e), enthalpy H (J kg^{-1}; Figure 6f), and velocity

https://doi.org/10.5194/egusphere-2026-913
Preprint. Discussion started: 16 March 2026

magnitude $|\boldsymbol{u}|$ (m a^{-1}; Figure 6g) at $t = 8.04$ ka (green dashed line), $t = 8.13$ ka (orange dashed line), and $t = 8.25$ ka (purple dashed line) in Figure 6a–6d). All four timeseries exhibit the low frequency oscillation with a period of ≈ 300 a, but the phase and shape of the oscillation vary between timeseries, with FT (Figure 6a) being the only quasi-symmetric oscillation. With more gradual rising limbs and steeper falling limbs, FT_b (Figure 6b) and $|\bar{\boldsymbol{u}}|$ (Figure 6d) are in phase with one another because the length of temperate bed (Figure 6b) directly governs the area that can be activated by the surge (Equation 20), thereby controlling the average speed attained by the surge (Figure 6d). For example, at $t = 8.04$ ka (Figure 6e.i, 6f.i, 6g.i) the extent of temperate bed (Figure 6b) and surge magnitude (Figure 6d) are at their minima, with extensional strain rates ($\dot{\varepsilon}_{xx} < 0$; Figure 6e.i) and high flow speeds (Figure 6g.i) confined to a limited reach along the flowline due to the limited extent of the temperate bed (Figure 6f.i).

Quantity h_ELA (Figure 6c) is antiphased with respect to FT_b (Figure 6b) and $|\bar{\boldsymbol{u}}|$ (Figure 6d). Variations in h_ELA are instructive for understanding variations in FT_b because the horizontal position of the ELA is the lower boundary of the latent heat pump (Equation 7 & 12; Figure 3), and therefore marks the location of the cold–temperate transition surface (CTS) at the glacier surface. Changes in h_ELA reflect changes in the flux of ice from the accumulation zone which controls the length and slope of the CTS (e.g. Figures 3 and 6f). When surges are confined to a limited reach of the glacier (e.g., when the length of temperate bed is at a minimum), each surge causes some thickening of the glacier at the ELA, eventually resulting in the h_ELA maximum illustrated by the green dashed line at $t = 8.04$ ka in Figure 6c. The increased h_ELA increases the flux of temperate ice from the accumulation zone which by $t = 8.13$ ka has caused the length of temperate bed to increase (Figure 6f.ii), in turn increasing the surge magnitude (Figure 6d & 6g.ii). Surges of increased magnitude and extent result in progressive thinning of the accumulation zone, as reflected in h_ELA (Figure 6c, between green and purple dashed lines), yielding the antiphase relationship between FT_b and h_ELA. By $t = 8.25$ ka, h_ELA, and therefore the flux of temperate ice, has decreased sufficiently that FT_b can no longer be sustained due to conductive cooling from the surface (note thin layer of temperate ice near the bed in Figure 6f.iii); thereafter, FT_b decreases dramatically (Figures 6b, after the purple dashed line) thereby restricting the extent of the subsequent surge. The near coincidence of troughs in FT and peaks in FT_b (Figure 6a & 6b) arises because the entire ice column must cool before FT_b decreases.

The position along the flowline of the dynamic balance line (DBL) relative to the ELA, is illustrative of how this oscillation occurs. On the rising limb of h_ELA (Figure 6c, green dotted line), the ELA is below the dynamic balance line and therefore falls within the receiving zone of the surge (Figure 6e.i, 6f.i, 6g.i) causing the step-line increases in h_ELA every 30a associated with the individual surge events. In the middle of the falling limb of h_ELA (Figure 6c, orange dotted line) the dynamic balance line is co-located with the ELA (Figure 6e.ii, 6f.ii, 6g.ii), and the abrupt changes in h_ELA nearly vanish. Toward the end of the falling limb of h_ELA (Figure 6c, leading up to the purple dotted line) the ELA is above the dynamic balance line (Figure 6e.iii, 6f.iii, 6g.iii) and thus falls within the reservoir zone, such that surges produce step-like decreases in h_ELA (Figure 6c). The drawdown at the ELA continues until h_ELA reaches a minimum (Figure 6c, after purple dotted line), at which time conductive cooling rapidly reduces FT_b (Figure 6b) and the cycle repeats itself.

https://doi.org/10.5194/egusphere-2026-913
Preprint. Discussion started: 16 March 2026

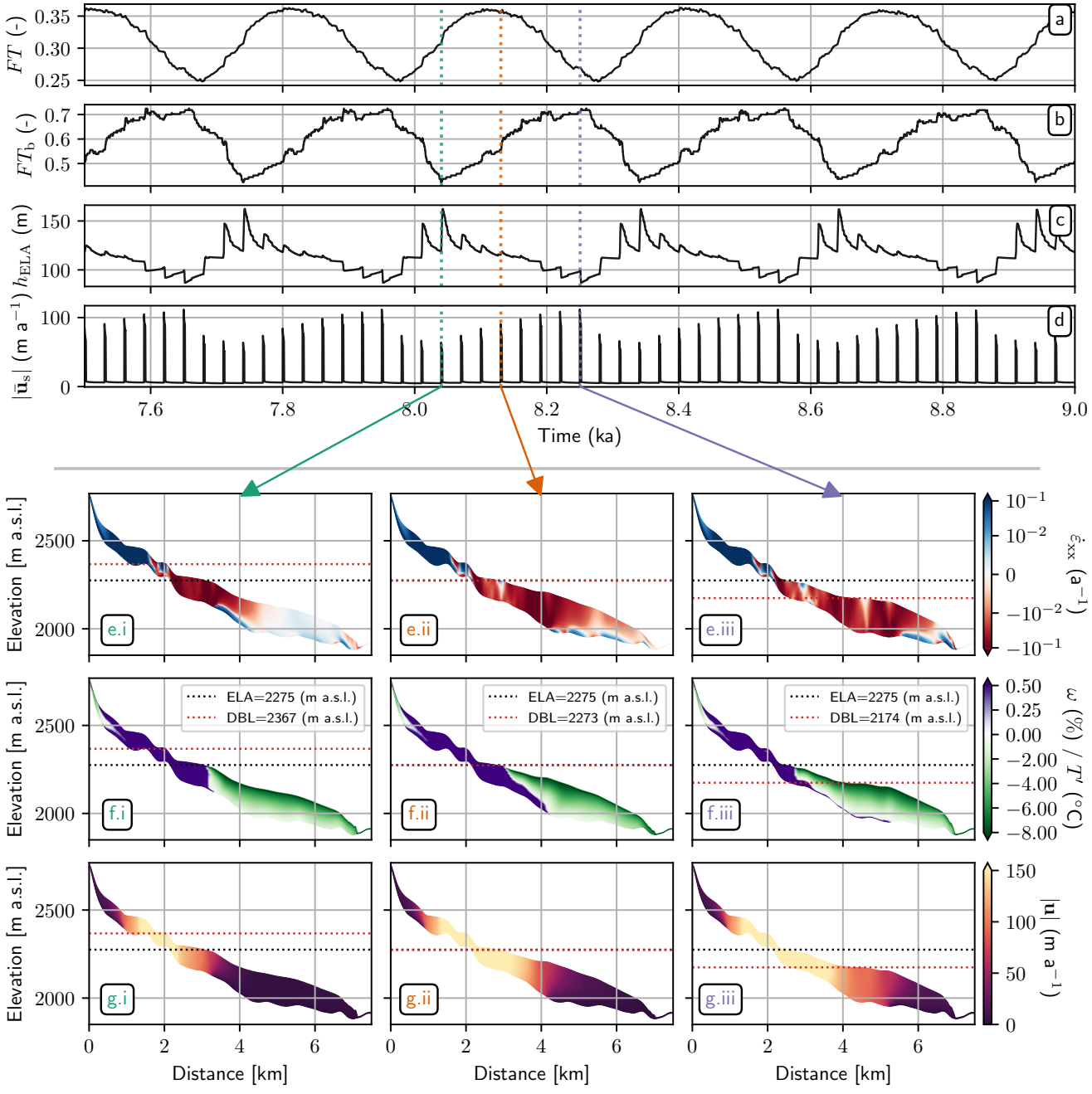

Figure 6. (a-d) Timeseries from 7.5–9.0 ka for $\beta^2 = 3.16 \times 10^{-4}$ m a^{-1} MPa^{-1} and $T_s = 30$ a. (a) Fraction temperate FT (−). (b) Fraction temperate bed FT_b (−). (c) Ice thickness at the ELA h_{ELA} (m). (d) Average surface speed $|\bar{\boldsymbol{u}}|$ (m a^{-1}). Vertical lines at $t = 8.04$ ka (green), $t = 8.13$ ka (orange), and $t = 8.25$ ka (purple) correspond to the three time slices shown in (e–g). The abrupt changes in (c) and (d) every 30 a correspond to the forced surges. (e–f) Distributed fields at (i) $t = 8.04$ ka, (ii) $t = 8.13$ ka, and (iii) $t = 8.25$ ka. (e) Longitudinal strain rate $\dot{\varepsilon}_{xx}$ (a^{-1}). (f) Water content (%; purple) and temperature relative to the pressure melting point (°C; green). (g) Velocity magnitude $|\boldsymbol{u}|$ (m a^{-1}). The dotted black and red horizontal lines represent, respectively, the ELA and the elevation of the dynamic balance line. All time slices represent the active phase of a surge.

https://doi.org/10.5194/egusphere-2026-913
Preprint. Discussion started: 16 March 2026

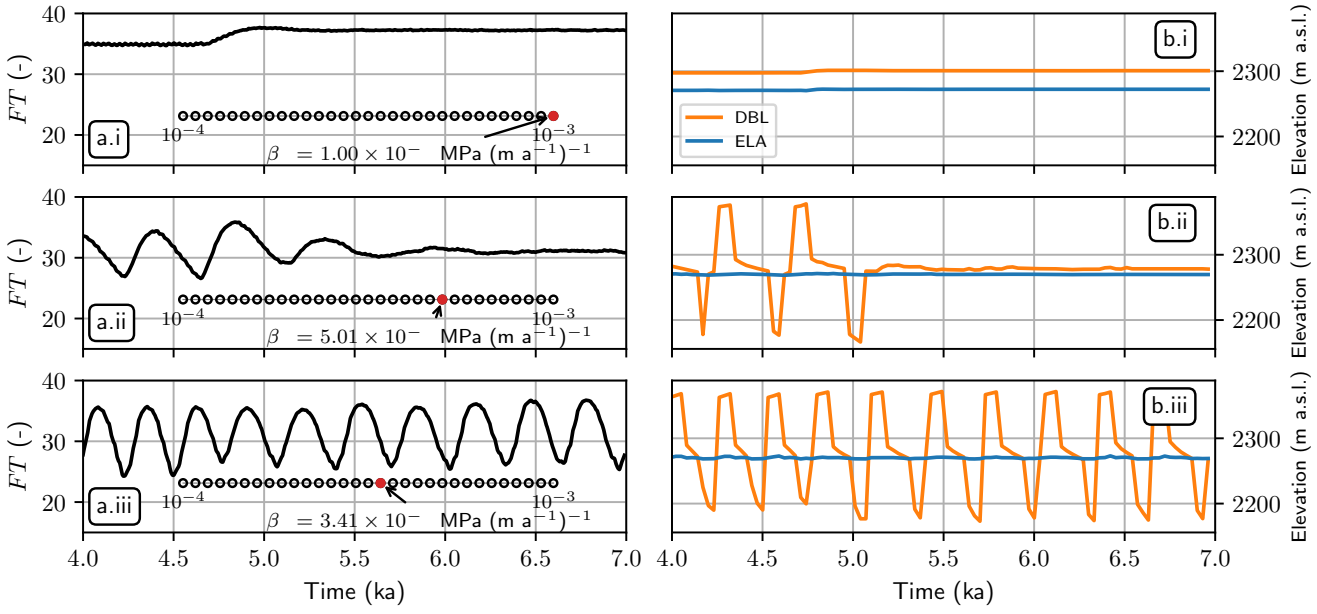

Figure 7. Emergence of secondary oscillations for surge period $T_s = 30$ a and select values of β^2. (a) Fraction temperate FT (−). Open circles on the logarithmic number line in (a) denote the full suite of β^2 values sampled, while red circles denote the individual β^2 values plotted in each row. (b) Elevation of the dynamic balance line (DBL, orange) and Equilibrium Line Altitude (ELA, blue) for simulations shown in (a) .

4.2.2 Oscillation emergence

To elucidate the conditions required for the secondary periodicity to emerge and be sustained, we again examine the $T_s = 30$ a simulations. The oscillation emerges when the value of β^2 is sufficiently low (Figure 5), corresponding to low values of basal friction and therefore high surge velocities. Such conditions give rise to high fluxes of temperate ice across the ELA during surges, and large associated changes in ice thickness, both of which exacerbate thermal disequilibrium between surges. This thermal disequilibrium is characterized by an extended temperate bed, which draws the dynamic balance line below the ELA, a condition required for the secondary oscillations to be sustained as described above.

For the oscillations to be maintained (Figure 7a), the glacier must be able to sustain vigorous enough surges that the DBL can propagate below the ELA at times (Figure 7b), while the thermodynamic feedbacks during quiescence must also allow the DBL to rise above the ELA at times. For some values of β^2, oscillations arise with the initial glacier geometry but then disappear as the glacier geometry adjusts to the negative mass-balance anomalies arising from the forced surges (Figure 7 a.ii & b.ii). Figure 7 b.ii illustrates a DBL that oscillates above and below the ELA until the oscillation becomes damped (prior to 5.5 ka), at which point the DBL remains just above the ELA.

https://doi.org/10.5194/egusphere-2026-913
Preprint. Discussion started: 16 March 2026

We examine the full suite of simulations to investigate variations in the emergence conditions as function of surge recurrence interval T_s. As T_s increases, more vigorous surges (driven by lower values of β^2) are required to initiate and sustain the oscillation. Longer surge return intervals allow for more recovery between surge events, producing thicker glaciers which in turn produce greater fluxes of temperate ice from the accumulation zone, leading to greater persistence of an extensive temperate bed. The net result is that lower values of β^2 are required to initiate oscillations in the presence of longer surge return intervals (Figure 8). For example, oscillations occur at $\beta^2 = 8.577 \times 10^{-4}$ m a^{-1} MPa^{-1} for $T_\mathrm{s} = 15$ a, whereas $\beta^2 = 4.29 \times 10^{-4}$ m a^{-1} MPa^{-1} is needed to initiate oscillations for $T_\mathrm{s} = 30$ and $\beta^2 = 2.51 \times 10^{-4}$ m a^{-1} MPa^{-1} for $T_\mathrm{s} = 60$.

4.2.3 Dependence of oscillation period and amplitude on surge vigor and return interval

Next, we examine the oscillation period as a function of surge vigor (controlled by β^2) and recurrence interval (T_s) (Figure 8). Oscillation period is calculated as the average distance between peaks in the FT timeseries from 6–9 ka in the simulations. Repeating the calculation with V' or $\bar{H}$ produced similar results. The oscillation period changes with β^2 and T_s because both parameters control the timescale over which the thinning of the accumulation zone occurs (Figure 8a). β^2 controls the flux during the surge—with lower values producing more vigorous surges—which is the mechanism that thins the ice column and initiates the oscillation.

Over the series of multiple surge events, the DBL moves below the ELA producing the oscillation as described in §4.2.2, while T_s defines the time between surges. Simulations with a longer recurrence interval T_s have a greater oscillation period (Figure 8a). At lower values of β^2, the oscillation periods appear nearly quantized (Figure 8a) owing to small differences in advection rates. Surge recurrence interval also produces significant variations in oscillation amplitude (Figure 8b), which is more difficult to reliably quantify and interpret than the variations in period. Amplitude varies non-monotonically with β^2, generally increasing at low values of β^2 (associated with the most vigorous surges) and then decreasing at higher values of β^2 (Figure 8b). The more complicated relationship between oscillation amplitude (as compared to period) and surge vigor is in part due to the small range of amplitudes (Figure 8), which themselves vary between oscillation cycles. The non-monotonic changes in FT near the peaks and troughs of the oscillation (Figure 5b), owing to the superimposed effects of surge events, further complicate the calculation of amplitude compared to period.

5 Discussion

5.1 Model simplifications and limitations

Given the idealized nature of this study, there are numerous simplifications in the model implementation and limitations to the experimental approach which we seek to enumerate here. The model simplifications include: our treatment of the firn aquifer (cf. Gilbert et al., 2014), omission of meltwater refreezing in crevasses and therefore a source of latent heat (cf. Jarvis and Clarke, 1974; Seguinot et al., 2020; Gilbert et al., 2020), use of a linear Weertman sliding law (cf. Gillet-Chaulet et al., 2016; Barnes and Gudmundsson, 2022), the idealized flowband geometry (cf. Sergienko, 2012), the lack of lateral drag parame-

https://doi.org/10.5194/egusphere-2026-913
Preprint. Discussion started: 16 March 2026

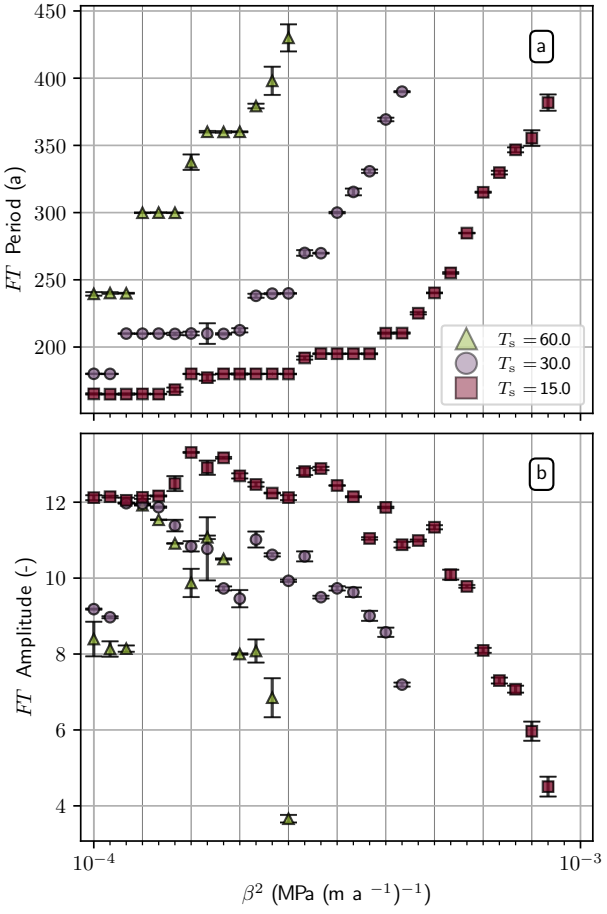

Figure 8. Fraction temperate (FT) oscillation (a) period and (b) amplitude as function of β^2 as assessed from 6–9 ka in the simulations. Periods remain unchanged when calculated with a different timeseries (e.g., $\bar{H}$).

terization (cf. Gagliardini et al., 2010), and small violations of mass conservation by neglecting the basal mass balance (cf. Aschwanden et al., 2012). Limitations of the experimental approach include: use of prescribed basal-friction perturbations that are instantaneous and occur over the full extent of the temperate bed to represent surge-like events, exploration of only a single glacier thermal structure, and use of a stationary climate forcing. Below we discuss the most important of these simplifications. For a more detailed discussion of all items see Nolan (2023).

5.1.1 Surface processes

The prescription of a constant firn-column thickness (Equation 13) and our simplified firn-aquifer parameterization (Equations 7–15) are too simplistic to capture temporal changes in the firn aquifer resulting from elevation-dependent feedbacks, which could produce hysteresis in thermal structure following a surge. A simplistic treatment of surface firn processes was necessitated

https://doi.org/10.5194/egusphere-2026-913
Preprint. Discussion started: 16 March 2026

by our use of a prescribed net mass balance (from Robinson et al. (2025)), rather than a surface process model that explicitly calculates accumulation, melt, and refreezing. Given the numerous simplifications made in our idealized approach, we deemed it preferable to use a prescribed mass-balance forcing that was realistic for the geographical area that inspired this work than to implement a surface-process model, which would require additional tuning. Our approach introduces conservation of mass violations, as the melt calculated as part of the meltwater refreezing scheme (Equation 7) is not explicitly coupled to the surface mass balance. Compared to the unresolved firn processes however, the above shortcoming has a negligible impact on our results as the steady-state thermal structure is insensitive to plausible changes in meltwater production. Future work would benefit from implementation of a surface process model that includes meltwater percolation in firn (e.g., Gilbert et al., 2012; Gilbert et al., 2020).

5.1.2 Forced surge events

While the use of forced surge events to study the effects of surging has a long history (e.g., Campbell and Rasmussen, 1969; Clarke, 1976; Aðalgeirsdóttir et al., 2014; Young et al., 2022), surges are not externally forced in reality but rather arise from an internal dynamic instability (e.g. Clarke, 1987). However, given the incomplete understanding of the physical mechanisms responsible for surge initiation (e.g. Minchew and Meyer, 2020; Thøgersen et al., 2019), prescribing perturbations in basal traction to elicit surge-like behavior seemed a reasonable choice given the focus of this study.

While we chose to prescribe surge events at a constant time interval (irrespective of glacier geometry), an alternative would have been to prescribe events when a mass-accumulation threshold is reached, mimicking some observations (e.g. Eisen et al., 2001). In this case, the surge recurrence interval would vary as a function of surge vigor (governed by the basal friction coefficient β^2) and the chosen accumulation threshold. Whether this approach would lead to the multidecadal surge-recurrence intervals characteristic of the Yukon glaciers that inspired this study remains untested. Initial attempts to implement a mass-accumulation threshold condition proved computationally costly, as the short timestep associated with surging ($\Delta t_{\mathrm{D}} = \Delta t_{\mathrm{T}} = 0.05$ a) was required for the entire transient simulation. The quasi-periodic nature of surge events (Meier and Post, 1969) has been attributed to a mass-accumulation threshold required to initiate surging which would be achieved at a roughly constant interval in a stationary climate. While some surge-type glaciers adjust their recurrence intervals to mass inputs (e.g. Eisen et al., 2001; Striberger et al., 2011), others continue to surge at a nearly constant recurrence interval (e.g. Abe and Furuya, 2015; Bevington and Copland, 2014; Nolan et al., 2021), irrespective of changes in mass balance. The observation of (nearly) constant recurrence intervals, especially under negative mass-balance conditions (e.g. Zemp et al., 2019; Young et al., 2021), lends some support to our approach.

An additional limitation of our approach is the instantaneous and spatially widespread nature of the prescribed changes in basal traction to initiate and terminate surging. In the absence of modelling progressive changes in basal traction (e.g. Young et al., 2022), we cannot realistically represent conditions leading up to a surge whereby protracted acceleration is observed in both temperate and polythermal glaciers (e.g. Frappé and Clarke, 2007; Jay-Allemand et al., 2011). Observations also show that surges initiate over a limited area of the reservoir zone and can propagate both up and down glacier (e.g. Altena et al., 2019). Properly simulating surge propagation during the active phase would not preclude oscillations from occurring, but it

https://doi.org/10.5194/egusphere-2026-913
Preprint. Discussion started: 16 March 2026

would likely complicate the relationship between surge vigor and oscillation emergence. Finally, in order to mimic quiescence, whereby restricted flux out of the reservoir zone leads to mass build up in excess of the climatological recovery from a surge event (e.g., Eisen et al., 2001), we have imposed a no-sliding condition at the glacier bed between surges rather than attempting to model multiple and more nuanced processes that might contribute to flow resistance (e.g. Flowers et al., 2011). Employing additional mechanics to restricted mass flux during quiescence would also restrict the flux of temperate ice, resulting in slightly colder quiescent conditions. Nevertheless, the basic thermal structure required for the oscillation to emerge would persist.

5.1.3 Flowband geometry

The use of a flowband geometry (i.e., the plain strain approximation) is the most significant simplification made in the model formulation. In response to bedrock bumps, flowband models not only overestimate velocity perturbations, but produce perturbations with different structures (e.g., different locations of the global maximum, different numbers of local maxima and minima) than their three-dimensional (3D) counterparts (Sergienko, 2012). By ignoring transverse variations in bed topography, bed undulations are assumed to be infinitely wide, meaning ice can only flow up and over the undulations, as compared to the more complicated over-and-around flow, which occurs in three dimensions (Sergienko, 2012). Furthermore, during surges, the transfer of stress to lateral margins (e.g. Schoof, 2005; Thøgersen et al., 2019) becomes an important component of the global force balance that was entirely neglected in our model formulation. Given the idealized (i.e., non site specific) nature of this study, flowband geometries were highly appealing so as to avoid site-specific 3D peculiarities of any individual glacier, along with the added benefit of being more computationally efficient than 3D models. If flowband models are used in similar future work, a lateral drag parameterization ought to be included (e.g., Gagliardini et al., 2010; Pimentel et al., 2010).

5.1.4 Glacier thermal structure

Finally, and perhaps most importantly, the scope of our findings are limited by having only simulated a single reference glacier geometry with a particular thermal structure (cf., Figure 1 from Irvine-Fynn et al., 2011), which is characteristic of small polythermal glaciers where significant meltwater refreezing in the accumulation zone occurs (e.g. Wilson and Flowers, 2013). From the surface-forcing gridsearch (§3.1), we show that the steady-state thermal structures are robust to large (~ 40 m) changes in mean ice thickness, and therefore commensurate changes in flux (Figure 3). The sensitivity test results (§3.3) indicate that the only way to alter the glacier thermal structure is to restrict or enhance the extent of surface melting which is not highly sensitive to modest changes in surge-reservoir size. A more realistic treatment of reservoir-zone formation as discussed in §5.1.2 would produce a thermal structure similar to, but slightly colder than, our result (Figure 6f.iii). Provided that the thermal structure remains fundamentally unchanged, we would still expect the secondary oscillations to emerge.

The environmental conditions needed to achieve the thermal structure used in this study are not unique to Yukon/Alaska but also occur in Svalbard (e.g. Sevestre et al., 2015; Lovell et al., 2026), another location with a high concentration of polythermal and surge-type glaciers (e.g. Jiskoot et al., 2000). While the thermal regimes of large surge-type glaciers in Yukon are largely unmeasured, polythermal conditions have been observed based on borehole measurements at Steele Glacier (Jarvis and Clarke, 1975), where vertically extensive cold ice in the upper reaches of the glacier was detected in multiple boreholes. Future work

https://doi.org/10.5194/egusphere-2026-913
Preprint. Discussion started: 16 March 2026

should prioritize both models and observations of thermal structure (e.g. Ochwat et al., 2021; Jacquemart et al., 2025) for a variety of glaciers spanning a realistic range of geometric characteristics and environmental settings.

5.2 Analogs to the secondary periodicity

Ice stream activation–stagnation cycles, initially formulated by MacAyeal (1993) as an internal mechanism for Heinrich Events (Heinrich, 1988), are an example of thermodynamically controlled oscillations. While representations of these cycles have varied from zero-dimensional lumped-parameter models (e.g., Robel et al., 2013) to complex ice-dynamic models (e.g., Marshall and Clarke, 1997; Feldmann and Levermann, 2017), the underlying mechanism is the same: the ice–bed interface oscillates between cold and temperate conditions, where ice streaming (i.e., sliding) is enabled during temperate conditions. The internal nature of the thermal oscillations and independence from atmospheric and oceanographic drivers (cf. Bassis et al., 2017; Mann et al., 2021) has hindered their ability to explain the observed relationship between Heinrich events, Dansgaard–Oeschger cycles, and variability in Atlantic meridional overturning circulation (Marcott et al., 2011). Nevertheless, the mechanism initially proposed by MacAyeal (1993) does serve to explain the past and present stagnation of ice streams along the Siple Coast of Antarctica (Robel et al., 2013) which appear to occur on shorter timescales than Heinrich Events (e.g. Catania et al., 2012).

Like ice stream activation–stagnation cycles, the period and amplitude of the oscillations we document are determined by the timescales of conductive cooling. But instead of ice-surface temperature, geothermal heat flux, and accumulation rates setting those timescales (MacAyeal, 1993; Robel et al., 2013), surge vigor (β^2) and the time interval between surge events (T_s) are the primary controls on the oscillations we document. Changes in ice-surface temperature, geothermal heat flux, and accumulation/ablation rates would likely shift the parameter envelope in which the oscillations emerge. The difference in controlling parameters, however, is a result of the *secondary* oscillations being superimposed on the (forced or primary) surge-cycle oscillations, whereas the ice-stream cycles arise as a primary (unforced) oscillation. Without the forced surge events, which enable the length of temperate bed to vary as a function of the position of the DBL versus the ELA, these glaciers would achieve a stable (i.e., non-oscillatory) steady state (§3.1).

5.3 Likelihood of observing the secondary periodicity

Given the simplifications (e.g., idealized flowline geometry, simplistic treatment of surface boundary processes) and limitations (e.g., forced surge events, stationary climate forcing) of our numerical modeling approach, one may question the likelihood of observing the secondary oscillations if not their existence. First and foremost, glacier response to real climate forcing may be expected to obscure these unforced secondary oscillations. The stationary climate forcing used in this study to isolate internal processes is unrepresentative of reality, including in Yukon now (e.g. Young et al., 2021) or in the recent (~ 1000 a) past (Porter et al., 2019). The presence of secondary oscillations, as modeled here, would be difficult to distinguish from long-term climate-driven changes, upon which glacier surges are superimposed. Furthermore, surge propensity and thermal structure are evolving with climate (e.g. Gilbert et al., 2012; Wilson et al., 2013; Delcourt et al., 2013), making our use of a stationary climate and forced surges even further from the present reality. Finally, given that climate-driven glacier mass deficits appear to undermine surge propensity and/or vigor (Dowdeswell et al., 1995; Copland et al., 2011; Bevington and Copland, 2014;

https://doi.org/10.5194/egusphere-2026-913
Preprint. Discussion started: 16 March 2026

Frappé and Clarke, 2007), it stands to reason that these deficits would also undermine the secondary oscillations, which depend on a threshold mass flux (Figure 7).

Even if these oscillations do occur, it would be difficult to identify them given that so few glaciers in any region including Yukon (cf., Nàłùdäy/Lowell Glacier (Bevington and Copland, 2014), Dän Zhùr/Donjek Glacier (Abe and Furuya, 2015; Kochtitzky et al., 2019), Fisher Glacier (Partington et al., 2025), and Tweedsmuir Glacier (Sharp, 2021)) have been observed over multiple surge cycles. For $T_s = 30$ a, ≈ 8 surge cycles occur over the shortest period of the secondary oscillation (Figure 8 b), which is many more surge cycles than have been directly observed at any individual glacier. Among the glaciers that have been observed over multiple surge cycles, it is not clear how many are polythermal, a pre-requisite for the secondary oscillations. While there is nothing in our model formulation that prohibits the secondary oscillations from occurring in other geographic locations with polythermal surge-type glaciers, for example Svalbard (e.g., Sevestre et al., 2015), longer recurrence intervals (Dowdeswell et al., 1991) mean even fewer glaciers would have been observed over multiple surge cycles, making any secondary oscillations more difficult to identify. It also remains to be seen whether the secondary oscillations emerge in glaciers with polythermal structures different than the those tested here.

Given the limitations of our numerical modeling approach, it is impossible to assert that these secondary oscillations occur in nature, let alone could be observed. We have, however, demonstrated that ice dynamics and thermodynamics can interact over multiple surge cycles and dramatically alter surge characteristics. What role steady-state or transient thermomechanical processes play in observed changes in surge characteristics (e.g., Frappé and Clarke, 2007; De Paoli and Flowers, 2009; Bevington and Copland, 2014) remains to be seen. Future work investigating the evolution of surge propensity in a changing climate should prioritize thermomechanical modeling in order to identify coupled processes that might alter surge characteristics. We have demonstrated one possible consequence of the relationship between the dynamic balance line and the equilibrium line altitude that may motivate more careful and widespread attention to this relationship in observational studies of surging glaciers. Cataloging the position and extent of the reservoir zone on surging glaciers, for example from maps of surface-elevation change through a surge cycle, may contribute to understanding observed variations in surge vigor.

6 Conclusions

Using a thermomechanically coupled Stokes model applied to a idealized flowband geometry meant to be representative of a small polythermal glacier in sub-Arctic Canada, we have investigated aspects of the interplay between glacier surging and thermal structure in the presence of a stationary climate. The steady-state reference glacier was characterized by a polythermal structure strongly influenced by meltwater entrapment, with a largely temperate accumulation area and cold ablation area. Surge-like perturbations were applied to the reference glacier by abruptly reducing basal friction where the bed is temperate at regular intervals (15, 30, 60 years). We found that glaciers become both smaller and colder with increasing surge vigor (controlled by the prescribed reduction in basal friction) and decreasing recurrence interval. When these surge-like events become sufficiently vigorous, a secondary oscillation emerges associated with oscillations in the extent of temperate bed which themselves arise because the timescale of thermodynamic recovery from a surge exceeds the prescribed surge return

https://doi.org/10.5194/egusphere-2026-913
Preprint. Discussion started: 16 March 2026

Variable	Description	Value	Units
–	Seconds per year	31536000	$\mathrm{s\,a^{-1}}$
T_0	Reference temperature	200	K
T_{ptr}	Temperature at triple point of water	273.16	K
P_{ptr}	Pressure at triple point of water	6.12×10^{-4}	MPa
$\mathcal{B}'$	Clausius-Clapeyron constant	9.8×10^{-2}	$\mathrm{K\,MPa^{-1}}$
L	Latent heat of fusion	3.33×10^{5}	$\mathrm{J\,kg^{-1}}$
ρ_{s}	Surface (snow) density	350	$\mathrm{kg\,m^{-3}}$
ρ_{f}	Pore-close-off density	830	$\mathrm{kg\,m^{-3}}$
ρ_{ice}	Density of ice	910	$\mathrm{kg\,m^{-3}}$
ρ_{w}	Density of water	1000	$\mathrm{kg\,m^{-3}}$
g	Acceleration due to gravity	9.756×10^{15}	$\mathrm{m\,a^{2}}$
n	Flowlaw exponent	3	–
T_*	Limit temperature	263.15	K
A^+	Flowlaw prefactor if $T'(H) > T_*$	9.12×10^{12}	$\mathrm{MPa^{-3}\,a^{-1}}$
A^-	Flowlaw prefactor if $T'(H) < T_*$	7.65×10^{23}	$\mathrm{MPa^{-3}\,a^{-1}}$
Q^+	Apparent activation energy if $T'(H) > T_*$	6×10^{4}	$\mathrm{J\,mol^{-1}}$
Q^-	Apparent activation energy if $T'(H) < T_*$	1.15×10^{5}	$\mathrm{J\,mol^{-1}}$
R	Ideal gas constant	8.31	$\mathrm{J\,mol^{-1}K^{-1}}$
κ_0	Temperate ice enthalpy diffusivity	3.295×10^{3}	$\mathrm{kg\,m^{-1}\,a^{-1}}$
Q_{geo}	Geothermal heat flux	1.73×10^{6}	$\mathrm{J\,m^{-2}\,a^{-1}}$

Table 1. Physical constants and fixed model parameters used throughout experiments below.

interval by one to two orders of magnitude. Slipperier beds were, in general, associated with shorter period, higher amplitude oscillations. The emergence of this secondary oscillation demonstrates, in principle, that ice dynamics and thermodynamics can interact over multiple surge cycles and dramatically alter surge characteristics. Whether such a phenomenon exists in a real (non-stationary) climate, let alone would be detectable, remains unknown. This result does, however, invite questions about whether observations of evolving surge characteristics are entirely attributable to changes in climate, mass balance and glacier geometry.

Code and data availability. Code developed for this study is available at https://github.com/andrewdnolan/thermal-structure

https://doi.org/10.5194/egusphere-2026-913
Preprint. Discussion started: 16 March 2026

Symbol	Description	Reference value	Test range	Units
f_{dd}	Degree-day factor for snow	6	1–8	$\mathrm{mm\,w.e.\,K^{-1}d^{-1}}$
h_ρ	Firn thickness	13	4–40	m
ω_{en}	Max englacial water content	1	0–3	%
ω_{aq}	Max firn aquifer water content	5	1–15	%
IC	Initial condition	0	−10–0	°C
N_{z}	Number of vertical layers	15	30	–

Table 2. Parameters varied in the sensitivity tests.

6.1 Physical Constants and Parameter Ranges

Author contributions. GF conceived of the project and worked closely with AN who was responsible for all aspects of project implementation, including writing the code, performing the analyses and making the figures. AN interpreted the results in consultation with GF and AA. AG reviewed the work at a previous stage and provided critical input on model-parameter settings. AN drafted the manuscript with input and revisions from GF, AA, AG.

Competing interests. The authors declare that they have no competing interests.

Acknowledgements. This work was inspired by glaciers situated in the Traditional Territories of the Kluane, White River and Champagne & Aishihik First Nations in southwest Yukon, Canada. Funding was provided by the Natural Sciences and Engineering Research Council of Canada and Simon Fraser University. This research was enabled in part by support provided by the Digital Research Alliance of Canada through the use of the Cedar computing system. No use of AI/LLMs was made in this project nor in the writing of this manuscript.

https://doi.org/10.5194/egusphere-2026-913
Preprint. Discussion started: 16 March 2026

References

Aðalgeirsdóttir, G., Aschwanden, A., Khroulev, C., Boberg, F., Mottram, R., Lucas-Picher, P., and Christensen, J.: Role of model initialization for projections of 21st-century Greenland Ice Sheet mass loss, Journal of Glaciology, 60, 782–794, https://doi.org/10.3189/2014JoG13J202, 2014.

Abe, T. and Furuya, M.: Winter speed-up of quiescent surge-type glaciers in Yukon, Canada, The Cryosphere, 9, 1183–1190, https://doi.org/10.5194/tc-9-1183-2015, 2015.

Adalgeirsdóttir, G., Björnsson, H., Pálsson, F., and Magnússon, E.: Analyses of a surging outlet glacier of Vatnajökull ice cap, Iceland, Annals of Glaciology, 42, 23–28, https://doi.org/10.3189/172756405781812934, 2005.

Altena, B., Scambos, T., Fahnestock, M., and Kääb, A.: Extracting recent short-term glacier velocity evolution over southern Alaska and the Yukon from a large collection of Landsat data, The Cryosphere, 13, 795–814, https://doi.org/10.5194/tc-13-795-2019, 2019.

Arendt, A., Luthcke, S., Larsen, C., Abdalati, W., Krabill, W., and Beedle, M.: Validation of high-resolution GRACE mascon estimates of glacier mass changes in the St Elias Mountains, Alaska, USA, using aircraft laser altimetry, Journal of Glaciology, 54, https://doi.org/10.3189/002214308787780067, 2008.

Aschwanden, A., Bueler, E., Khroulev, C., and Blatter, H.: An enthalpy formulation for glaciers and ice sheets, Journal of Glaciology, 58, 441–457, https://doi.org/10.3189/2012JoG11J088, 2012.

Aschwanden, A., Fahnestock, M. A., Truffer, M., Brinkerhoff, D. J., Hock, R., Khroulev, C., Mottram, R., and Khan, S. A.: Contribution of the Greenland Ice Sheet to sea level over the next millennium, Science Advances, 5, https://doi.org/10.1126/sciadv.aav9396, 2019.

Barnes, J. M. and Gudmundsson, G. H.: The predictive power of ice sheet models and the regional sensitivity of ice loss to basal sliding parameterisations: a case study of Pine Island and Thwaites glaciers, West Antarctica, The Cryosphere, 16, 4291–4304, https://doi.org/10.5194/tc-16-4291-2022, 2022.

Bassis, J. N., Petersen, S. V., and Mac Cathles, L.: Heinrich events triggered by ocean forcing and modulated by isostatic adjustment, Nature, 542, 332–334, https://doi.org/10.1038/nature21069, 2017.

Bazai, N. A., Cui, P., Carling, P. A., Wang, H., Hassan, J., Liu, D., Zhang, G., and Jin, W.: Increasing glacial lake outburst flood hazard in response to surge glaciers in the Karakoram, Earth-Science Reviews, 212, 103 432, https://doi.org/10.1016/j.earscirev.2020.103432, 2021.

Benn, D. I., Fowler, A. C., Hewitt, I., and Sevestre, H.: A general theory of glacier surges, Journal of Glaciology, 65, 701–716, https://doi.org/10.1017/jog.2019.62, 2019.

Berthier, E., Schiefer, E., Clarke, G. K. C., Menounos, B., and Rémy, F.: Contribution of Alaskan glaciers to sea-level rise derived from satellite imagery, Nature Geoscience, 3, 92–95, https://doi.org/10.1038/ngeo737, 2010.

Bevington, A. and Copland, L.: Characteristics of the last five surges of Lowell Glacier, Yukon, Canada, since 1948, Journal of Glaciology, 60, 113–123, https://doi.org/10.3189/2014JoG13J134, 2014.

Björnsson, H.: Understanding jökulhlaups: From tale to theory, Journal of Glaciology, 56, 1002–1010, https://doi.org/10.3189/002214311796406086, 2010.

Calov, R. and Greve, R.: A semi-analytical solution for the positive degree-day model with stochastic temperature variations, Journal of Glaciology, 51, 173–175, https://doi.org/10.3189/172756505781829601, 2005.

Campbell, W. J. and Rasmussen, L. A.: Three-dimensional surges and recoveries in a numerical glacier model, Canadian Journal of Earth Sciences, 6, 979–986, https://doi.org/10.1139/e69-102, 1969.

https://doi.org/10.5194/egusphere-2026-913
Preprint. Discussion started: 16 March 2026

Catania, G., Hulbe, C., Conway, H., Scambos, T., and Raymond, C.: Variability in the mass flux of the Ross ice streams, West Antarctica, over the last millennium, Journal of Glaciology, 58, 741–752, https://doi.org/10.3189/2012JoG11J219, 2012.

Clarke, G.: Fast glacier flow: Ice streams, surging, and tidewater glaciers, Journal of Geophysical Research, 92, 8835–8841, https://doi.org/10.1029/JB092iB09p08835, 1987.

Clarke, G. K. and Blake, E. W.: Geometric and thermal evolution of a surge-type glacier in its quiescent state: Trapridge Glacier, Yukon Territory, Canada, 1969–89, Journal of Glaciology, 37, 158–169, https://doi.org/10.3189/S002214300004291X, 1991.

Clarke, G. K. C.: Thermal regulation of glacier surging, Journal of Glaciology, 16, 231–250, https://doi.org/10.1017/S0022143000031567, 1976.

Clarke, G. K. C. and Goodman, R. H.: Radio Echo Soundings and Ice-Temperature Measurements in a Surge-Type Glacier, Journal of Glaciology, 14, 71–78, https://doi.org/10.3189/S002214300001340X, 1975.

Clarke, G. K. C., Schmok, J. P., Ommanney, C. S. L., and Collins, S. G.: Characteristics of surge-type glaciers, Journal of Geophysical Research: Solid Earth, 91, 7165–7180, https://doi.org/10.1029/JB091iB07p07165, 1986.

Copland, L., Sylvestre, T., Bishop, M., F. Shroder, J., Seong, Y. B., Owen, L., Bush, A., and Kamp, U.: Expanded and recently increased glacier surging in the Karakoram, Arctic Antarctic and Alpine Research, 43, 503–516, https://doi.org/10.1657/1938-4246-43.4.503, 2011.

Crompton, J. W. and Flowers, G. E.: Correlations of suspended sediment size with bedrock lithology and glacier dynamics, Annals of Glaciology, 57, 142–150, https://doi.org/10.1017/aog.2016.6, 2016.

Cuffey, K. M. and Paterson, W. S. B.: The Physics of Glaciers, Academic Press, 4th edn., 2010.

De Paoli, L. and Flowers, G.: Dynamics of a small surge-type glacier using one-dimensional geophysical inversion, Journal of Glaciology, 55, https://doi.org/10.3189/002214309790794850, 2009.

Delcourt, C., Van Liefferinge, B., Nolan, M., and Pattyn, F.: The climate memory of an Arctic polythermal glacier, Journal of Glaciology, 59, 1084–1092, https://doi.org/10.3189/2013JoG12J109, 2013.

Dowdeswell, J., Hodgkins, R., Nuttall, A.-M., Hagen, J., and Hamilton, G.: Mass balance change as a control on the frequency and occurrence of glacier surges in Svalbard, Norwegian High Arctic, Geophysical Research Letters, 22, 2909–2912, https://doi.org/10.1029/95GL02821, 1995.

Dowdeswell, J. A., Hamilton, G. S., and Hagen, J. O.: The duration of the active phase on surge-type glaciers: contrasts between Svalbard and other regions, Journal of Glaciology, 37, 388–400, https://doi.org/10.3189/S0022143000005827, 1991.

Eisen, O., Harrison, W. D., and Raymond, C. F.: The surges of Variegated Glacier, Alaska, U.S.A., and their connection to climate and mass balance, Journal of Glaciology, 47, 351–358, https://doi.org/10.3189/172756501781832179, 2001.

Farinotti, D., Huss, M., Fürst, J. J., Landmann, J., Machguth, H., Maussion, F., and Pandit, A.: A consensus estimate for the ice thickness distribution of all glaciers on Earth, Nature Geoscience, 12, 168–173, https://doi.org/10.1038/s41561-019-0300-3, 2019.

Feldmann, J. and Levermann, A.: From cyclic ice streaming to Heinrich-like events: the grow-and-surge instability in the Parallel Ice Sheet Model, The Cryosphere, 11, 1913–1932, https://doi.org/10.5194/tc-11-1913-2017, 2017.

Flowers, G., Roux, N., Pimentel, S., and Schoof, C.: Present dynamics and future prognosis of a slowly surging glacier, The Cryosphere, 5, 299–313, https://doi.org/10.5194/tc-5-299-2011, 2011.

Fowler, A. C.: On the transport of moisture in polythermal glaciers, Geophysical & Astrophysical Fluid Dynamics, 28, 99–140, https://doi.org/10.1080/03091928408222846, 1984.

Fowler, A. C., Murray, T., and Ng, F. S. L.: Thermally controlled glacier surging, Journal of Glaciology, 47, 527–538, https://doi.org/10.3189/172756501781831792, 2001.

https://doi.org/10.5194/egusphere-2026-913
Preprint. Discussion started: 16 March 2026

Fowler, J. R. and Iverson, N. R.: A permeameter for temperate ice: first results on permeability sensitivity to grain size, Journal of Glaciology, 68, 764–774, https://doi.org/10.1017/jog.2021.136, 2022.

Frappé, T.-P. and Clarke, G. K. C.: Slow surge of Trapridge Glacier, Yukon Territory, Canada, Journal of Geophysical Research: Earth Surface, 112, https://doi.org/10.1029/2006JF000607, 2007.

Gagliardini, O., Durand, G., Zwinger, T., Hindmarsh, R. C. A., and Le Meur, E.: Coupling of ice-shelf melting and buttressing is a key process in ice-sheets dynamics, Geophysical Research Letters, 37, https://doi.org/https://doi.org/10.1029/2010GL043334, 2010.

Gagliardini, O., Zwinger, T., Gillet-Chaulet, F., Durand, G., Favier, L., de Fleurian, B., Greve, R., Malinen, M., Martín, C., Råback, P., Ruokolainen, J., Sacchettini, M., Schäfer, M., Seddik, H., and Thies, J.: Capabilities and performance of Elmer/Ice, a new-generation ice sheet model, Geoscientific Model Development, 6, 1299–1318, https://doi.org/10.5194/gmd-6-1299-2013, 2013.

Gilbert, A., Vincent, C., Wagnon, P., Thibert, E., and Rabatel, A.: The influence of snow cover thickness on the thermal regime of Tête Rousse Glacier (Mont Blanc range, 3200 m a.s.l.): Consequences for outburst flood hazards and glacier response to climate change, Journal of Geophysical Research: Earth Surface, 117, https://doi.org/10.1029/2011JF002258, 2012.

Gilbert, A., Gagliardini, O., Vincent, C., and Wagnon, P.: A 3-D thermal regime model suitable for cold accumulation zones of polythermal mountain glaciers, Journal of Geophysical Research: Earth Surface, 119, 1876–1893, https://doi.org/https://doi.org/10.1002/2014JF003199, 2014.

Gilbert, A., Sinisalo, A., Gurung, T. R., Fujita, K., Maharjan, S. B., Sherpa, T. C., and Fukuda, T.: The influence of water percolation through crevasses on the thermal regime of a Himalayan mountain glacier, The Cryosphere, 14, 1273–1288, https://doi.org/10.5194/tc-14-1273-2020, 2020.

Gillet-Chaulet, F., Durand, G., Gagliardini, O., Mosbeux, C., Mouginot, J., Rémy, F., and Ritz, C.: Assimilation of surface velocities acquired between 1996 and 2010 to constrain the form of the basal friction law under Pine Island Glacier, Geophysical Research Letters, 43, 10,311–10,321, https://doi.org/https://doi.org/10.1002/2016GL069937, 2016.

Greve, R. and Blatter, H.: Dynamics of Ice Sheets and Glaciers, Advances in Geophysical and Environmental Mechanics and Mathematics, Springer Berlin Heidelberg, Berlin, Heidelberg, 2009.

Gusmeroli, A., Jansson, P., Pettersson, R., and Murray, T.: Twenty years of cold surface layer thinning at Storglaciären, sub-Arctic Sweden, 1989–2009, Journal of Glaciology, 58, 3–10, https://doi.org/10.3189/2012JoG11J018, 2012.

Haseloff, M., Hewitt, I. J., and Katz, R. F.: Englacial Pore Water Localizes Shear in Temperate Ice Stream Margins, Journal of Geophysical Research: Earth Surface, 124, 2521–2541, https://doi.org/10.1029/2019JF005399, 2019.

Heinrich, H.: Origin and Consequences of Cyclic Ice Rafting in the Northeast Atlantic Ocean During the Past 130,000 Years, Quaternary Research, 29, 142–152, https://doi.org/10.1016/0033-5894(88)90057-9, 1988.

Hill, E. A., Rosier, S. H. R., Gudmundsson, G. H., and Collins, M.: Quantifying the potential future contribution to global mean sea level from the Filchner–Ronne basin,Antarctica, The Cryosphere, 15, 4675–4702, https://doi.org/10.5194/tc-15-4675-2021, 2021.

Hock, R.: A distributed temperature-index ice- and snowmelt model including potential direct solar radiation, Journal of Glaciology, 45, 101–111, https://doi.org/10.3189/S0022143000003087, 1999.

Irvine-Fynn, T. D. L., Hodson, A. J., Moorman, B. J., Vatne, G., and Hubbard, A. L.: Polythermal glacier hydrology: A review, Reviews of Geophysics, 49, RG4002, https://doi.org/10.1029/2010RG000350, 2011.

Jacquemart, M., Welty, E., Gastaldello, M., and Carcanade, G.: glenglat: a database of global englacial temperatures, Earth System Science Data, 17, 1627–1666, https://doi.org/10.5194/essd-17-1627-2025, 2025.

https://doi.org/10.5194/egusphere-2026-913
Preprint. Discussion started: 16 March 2026

Jarvis, G. T. and Clarke, G. K. C.: Thermal Effects of Crevassing on Steele Glacier, Yukon Territory, Canada, Journal of Glaciology, 13, 243–254, https://doi.org/10.3189/S0022143000023054, 1974.

Jarvis, G. T. and Clarke, G. K. C.: The Thermal Regime of Trapridge Glacier and its Relevance to Glacier Surging, Journal of Glaciology, 14, 235–250, https://doi.org/10.3189/S0022143000021729, 1975.

Jay-Allemand, M., Gillet-Chaulet, F., Gagliardini, O., and Nodet, M.: Investigating changes in basal conditions of Variegated Glacier prior to and during its 1982–1983 surge, The Cryosphere, 5, 659–672, https://doi.org/10.5194/tc-5-659-2011, 2011.

Jiskoot, H., Murray, T., and Boyle, P.: Controls on the distribution of surge-type glaciers in Svalbard, Journal of Glaciology, 46, 412–422, https://doi.org/10.3189/172756500781833115, 2000.

King, O., Bhattacharya, A., and Bolch, T.: The presence and influence of glacier surging around the Geladandong ice caps, North East Tibetan Plateau, Advances in Climate Change Research, 12, 299–312, https://doi.org/10.1002/2015JF003517, 2021.

Kochtitzky, W., Jiskoot, H., Copland, L., Enderlin, E., McNabb, R., Kreutz, K., and Main, B.: Terminus advance, kinematics and mass redistribution during eight surges of Donjek Glacier, St. Elias Range, Canada, 1935 to 2016, Journal of Glaciology, 65, 565–579, https://doi.org/10.1017/jog.2019.34, 2019.

Lovell, H., Benn, D. I., Jiskoot, H., Stokes, C. R., Flowers, G. E., Guillet, G., Mannerfelt, E. S., Falaschi, D., Kääb, A., King, O., Benediktsson, I. O., Bhambri, R., Lv, M., Muhammad, S., and Luckman, A.: Glacier surging and surge-related hazards in a changing climate, Nature Reviews Earth and Environment, https://doi.org/10.1038/s43017-025-00757-9, 2026.

MacAyeal, D. R.: Binge/purge oscillations of the Laurentide Ice Sheet as a cause of the North Atlantic's Heinrich events, Paleoceanography, 8, 775–784, https://doi.org/10.1029/93PA02200, 1993.

Mann, L. E., Robel, A. A., and Meyer, C. R.: Synchronization of Heinrich and Dansgaard-Oeschger Events Through Ice-Ocean Interactions, Paleoceanography and Paleoclimatology, 36, https://doi.org/10.1002/essoar.10507501.1, 2021.

Marcott, S. A., Clark, P. U., Padman, L., Klinkhammer, G. P., Springer, S. R., Liu, Z., Otto-Bliesner, B. L., Carlson, A. E., Ungerer, A., Padman, J., He, F., Cheng, J., and Schmittner, A.: Ice-shelf collapse from subsurface warming as a trigger for Heinrich events, Proceedings of the National Academy of Sciences, 108, 13 415–13 419, https://doi.org/10.1073/pnas.1104772108, 2011.

Marshall, S. J. and Clarke, G. K. C.: A continuum mixture model of ice stream thermomechanics in the Laurentide Ice Sheet 2. Application to the Hudson Strait Ice Stream, Journal of Geophysical Research: Solid Earth, 102, 20 615–20 637, https://doi.org/10.1029/97JB01189, 1997.

Maussion, F., Butenko, A., Champollion, N., Dusch, M., Eis, J., Fourteau, K., Gregor, P., Jarosch, A. H., Landmann, J., Oesterle, F., Recinos, B., Rothenpieler, T., Vlug, A., Wild, C. T., and Marzeion, B.: The Open Global Gacier Model (OGGM) v1.1, Geoscientific Model Development, 2019, 909–931, https://doi.org/10.5194/gmd-12-909-2019, 2019.

Meier, M. F. and Post, A.: What are glacier surges?, Canadian Journal of Earth Sciences, 6, 807–817, https://doi.org/10.1139/e69-081, 1969.

Meier, M. F. and Post, A.: Fast tidewater glaciers, Journal of Geophysical Research: Solid Earth, 92, 9051–9058, https://doi.org/10.1029/JB092iB09p09051, 1987.

Minchew, B. M. and Meyer, C. R.: Dilation of subglacial sediment governs incipient surge motion in glaciers with deformable beds, Proceedings of the Royal Society A: Mathematical, Physical and Engineering Sciences, 476, 20200 033, https://doi.org/10.1098/rspa.2020.0033, 2020.

Morin, A., Flowers, G. E., Nolan, A., Brinkerhoff, D., and Berthier, E.: Exploiting high-slip flow regimes to improve inference of glacier bed topography, Journal of Glaciology, p. 1–7, https://doi.org/10.1017/jog.2022.121, 2023.

https://doi.org/10.5194/egusphere-2026-913
Preprint. Discussion started: 16 March 2026

Murray, T., Stuart, G. W., Miller, P. J., Woodward, J., Smith, A. M., Porter, P. R., and Jiskoot, H.: Glacier surge propagation by thermal evolution at the bed, Journal of Geophysical Research: Solid Earth, 105, 13 491–13 507, https://agupubs.onlinelibrary.wiley.com/doi/abs/10.1029/2000JB900066, 2000.

Murray, T., Strozzi, T., Luckman, A., Jiskoot, H., and Christakos, P.: Is there a single surge mechanism? Contrasts in dynamics between glacier surges in Svalbard and other regions, Journal of Geophysical Research: Solid Earth, 108, https://doi.org/10.1029/2002JB001906, 2003.

Nolan, A.: Thermomechanically coupled modeling of polythermal glacier response to surge-like perturbations, Master's thesis, 2023.

Nolan, A., Kochtitzky, W., Enderlin, E. M., McNabb, R., and Kreutz, K. J.: Kinematics of the exceptionally-short surge cycles of Sít' Kusá (Turner Glacier), Alaska, from 1983 to 2013, Journal of Glaciology, 67, 744–758, https://doi.org/10.1017/jog.2021.29, 2021.

Nuth, C., Moholdt, G., Kohler, J., Hagen, J. O., and Kääb, A.: Svalbard glacier elevation changes and contribution to sea level rise, Journal of Geophysical Research: Earth Surface, 115, https://doi.org/10.1029/2008JF001223, 2010.

Ochwat, N. E., Marshall, S. J., Moorman, B. J., Criscitiello, A. S., and Copland, L.: Evolution of the firn pack of Kaskawulsh Glacier, Yukon: meltwater effects, densification, and the development of a perennial firn aquifer, The Cryosphere, 15, 2021–2040, https://doi.org/10.5194/tc-15-2021-2021, 2021.

Oster, S. E. and Albert, M. R.: Thermal conductivity of polar firn, Journal of Glaciology, p. 1–8, https://doi.org/10.1017/jog.2022.28, 2022.

Partington, G., Copland, L., Lauzon, B., Medrzycka, D., Main, B., Kochtitzky, W. H., and Dow, C. F.: Surge history and dynamics of Fisher Glacier, Yukon, 1948–2022, Journal of Glaciology, 71, e100, https://doi.org/10.1017/jog.2025.10084, 2025.

Pimentel, S., Flowers, G. E., and Schoof, C. G.: A hydrologically coupled higher-order flow-band model of ice dynamics with a Coulomb friction sliding law, Journal of Geophysical Research: Earth Surface, 115, https://doi.org/10.1029/2009JF001621, 2010.

Porter, T. J., Schoenemann, S. W., Davies, L. J., Steig, E. J., Bandara, S., and Froese, D. G.: Recent summer warming in northwestern Canada exceeds the Holocene thermal maximum, Nature Communications, 10, 1631, https://doi.org/10.1038/s41467-019-09622-y, 2019.

Rizzoli, P., Martone, M., Gonzalez, C., Wecklich, C., Borla Tridon, D., Bräutigam, B., Bachmann, M., Schulze, D., Fritz, T., Huber, M., Wessel, B., Krieger, G., Zink, M., and Moreira, A.: Generation and performance assessment of the global TanDEM-X digital elevation model, ISPRS Journal of Photogrammetry and Remote Sensing, 132, 119–139, https://doi.org/10.1016/j.isprsjprs.2017.08.008, 2017.

Robel, A. A., DeGiuli, E., Schoof, C., and Tziperman, E.: Dynamics of ice stream temporal variability: Modes, scales, and hysteresis, Journal of Geophysical Research: Earth Surface, 118, 925–936, https://doi.org/10.1002/jgrf.20072, 2013.

Robinson, K. M., Flowers, G. E., and Rounce, D. R.: Sensitivity of modelled mass balance and runoff to representations of debris and accumulation on the Kaskawulsh Glacier, Yukon, Canada, Journal of Glaciology, 71, e42, https://doi.org/10.1017/jog.2025.8, 2025.

Round, V., Leinss, S., Huss, M., Haemmig, C., and Hajnsek, I.: Surge dynamics and lake outbursts of Kyagar Glacier, Karakoram, The Cryosphere, 11, 723–739, https://doi.org/10.5194/tc-11-723-2017, 2017.

Råback, P.: ElmerGrid Manual, CSC – IT Center for Science, https://www.nic.funet.fi/pub/sci/physics/elmer/doc/ElmerGridManual.pdf, 2023.

Schoof, C.: The effect of cavitation on glacier sliding, Proceedings of the Royal Society A: Mathematical, Physical and Engineering Sciences, 461, 609–627, https://doi.org/10.1098/rspa.2004.1350, 2005.

Schoof, C. and Hewitt, I. J.: A model for polythermal ice incorporating gravity-driven moisture transport, Journal of Fluid Mechanics, 797, 504–535, https://doi.org/10.1017/jfm.2016.251, 2016.

Seguinot, J., Funk, M., Bauder, A., Wyder, T., Senn, C., and Sugiyama, S.: Englacial warming indicates deep crevassing in Bowdoin Glacier, Greenland, Frontiers in Earth Science, 8, 65, https://doi.org/10.3389/feart.2020.00065, 2020.

https://doi.org/10.5194/egusphere-2026-913
Preprint. Discussion started: 16 March 2026

Sergienko, O. V.: The effects of transverse bed topography variations in ice-flow models, Journal of Geophysical Research: Earth Surface, 117, https://doi.org/https://doi.org/10.1029/2011JF002203, 2012.

Sevestre, H. and Benn, D. I.: Climatic and geometric controls on the global distribution of surge-type glaciers: implications for a unifying model of surging, Journal of Glaciology, 61, 646–662, https://doi.org/10.3189/2015JoG14J136, 2015.

Sevestre, H., Benn, D. I., Hulton, N. R. J., and Bælum, K.: Thermal structure of Svalbard glaciers and implications for thermal switch models of glacier surging, Journal of Geophysical Research: Earth Surface, 120, 2220–2236, https://doi.org/10.1002/2015JF003517, 2015.

Sharp, M.: Amplification of Surface Topography during Surges of Tweedsmuir Glacier, Master's thesis, University of Calgary, 2021.

Striberger, J., Björck, S., Benediktsson, I. O., Snowball, I., Uvo, C. B., Ingólfsson, O., and Kjær, K. H.: Climatic control of the surge periodicity of an Icelandic outlet glacier, Journal of Quaternary Science, 26, 561–565, https://doi.org/10.1002/jqs.1527, 2011.

Thøgersen, K., Gilbert, A., Schuler, T. V., and Malthe-Sørenssen, A.: Rate-and-state friction explains glacier surge propagation, Nature Communications, 10, 2823, https://doi.org/10.1038/s41467-019-10506-4, 2019.

Truffer, M., Kääb, A., Harrison, W. D., Osipova, G. B., Nosenko, G. A., Espizua, L., Gilbert, A., Fischer, L., Huggel, C., Craw Burns, P. A., and Lai, A. W.: Chapter 13 - Glacier surges, in: Snow and Ice-Related Hazards, Risks, and Disasters (Second Edition), edited by Haeberli, W. and Whiteman, C., Hazards and Disasters Series, pp. 417–466, Elsevier, second edition edn., https://doi.org/10.1016/B978-0-12-817129-5.00003-2, 2021.

Virtanen, P., Gommers, R., Oliphant, T. E., Haberland, M., Reddy, T., Cournapeau, D., Burovski, E., Peterson, P., Weckesser, W., Bright, J., van der Walt, S. J., Brett, M., Wilson, J., Millman, K. J., Mayorov, N., Nelson, A. R. J., Jones, E., Kern, R., Larson, E., Carey, C. J., Polat, İ., Feng, Y., Moore, E. W., VanderPlas, J., Laxalde, D., Perktold, J., Cimrman, R., Henriksen, I., Quintero, E. A., Harris, C. R., Archibald, A. M., Ribeiro, A. H., Pedregosa, F., van Mulbregt, P., and SciPy 1.0 Contributors: SciPy 1.0: Fundamental Algorithms for Scientific Computing in Python, Nature Methods, 17, 261–272, https://doi.org/10.1038/s41592-019-0686-2, 2020.

Wilson, N. and Flowers, G.: Environmental controls on the thermal structure of alpine glaciers, The Cryosphere, Volume 7, Issue 1, 2013, pp.167-182, 7, 167–182, https://doi.org/10.5194/tc-7-167-2013, 2013.

Wilson, N., Flowers, G., and Mingo, L.: Comparison of thermal structure and evolution between neighboring subarctic glaciers, Journal of Geophysical Research: Earth Surface, 118, 1443–1459, https://doi.org/10.1002/jgrf.20096, 2013.

Young, E. M., Flowers, G. E., Berthier, E., and Latto, R.: An imbalancing act: the delayed dynamic response of the Kaskawulsh Glacier to sustained mass loss, Journal of Glaciology, 67, 313–330, https://doi.org/10.1017/jog.2020.107, 2021.

Young, E. M., Flowers, G. E., Jiskoot, H., and Gibson, H. D.: Kinematic evolution of kilometre-scale fold trains in surge-type glaciers explored with a numerical model, Journal of Structural Geology, 161, 104 644, https://doi.org/https://doi.org/10.1016/j.jsg.2022.104644, 2022.

Zemp, M., Huss, M., Thibert, E., Eckert, N., Mcnabb, R., Huber, J., Barandun, M., Machguth, H., Nussbaumer, S. U., Thomson, L., Paul, F., Maussion, F., Kutuzov, S., and Cogley, J. G.: Global glacier mass changes and their contributions to sea-level rise from 1961 to 2016, Nature, 568, 382–386, https://doi.org/10.1038/s41586-019-1071-0, 2019.

Zwinger, T., Greve, R., Gagliardini, O., Shiraiwa, T., and Lyly, M.: A full Stokes-flow thermo-mechanical model for firn and ice applied to the Gorshkov crater glacier, Kamchatka, Annals of Glaciology, 45, 29–37, https://doi.org/10.3189/172756407782282543, 2007.